Synthesis, stability tests and irradiation evaluation of hollow MoS_2 nanomaterials

With applications in a new circular low-activity technetium-99m generator

Caro van Dijk

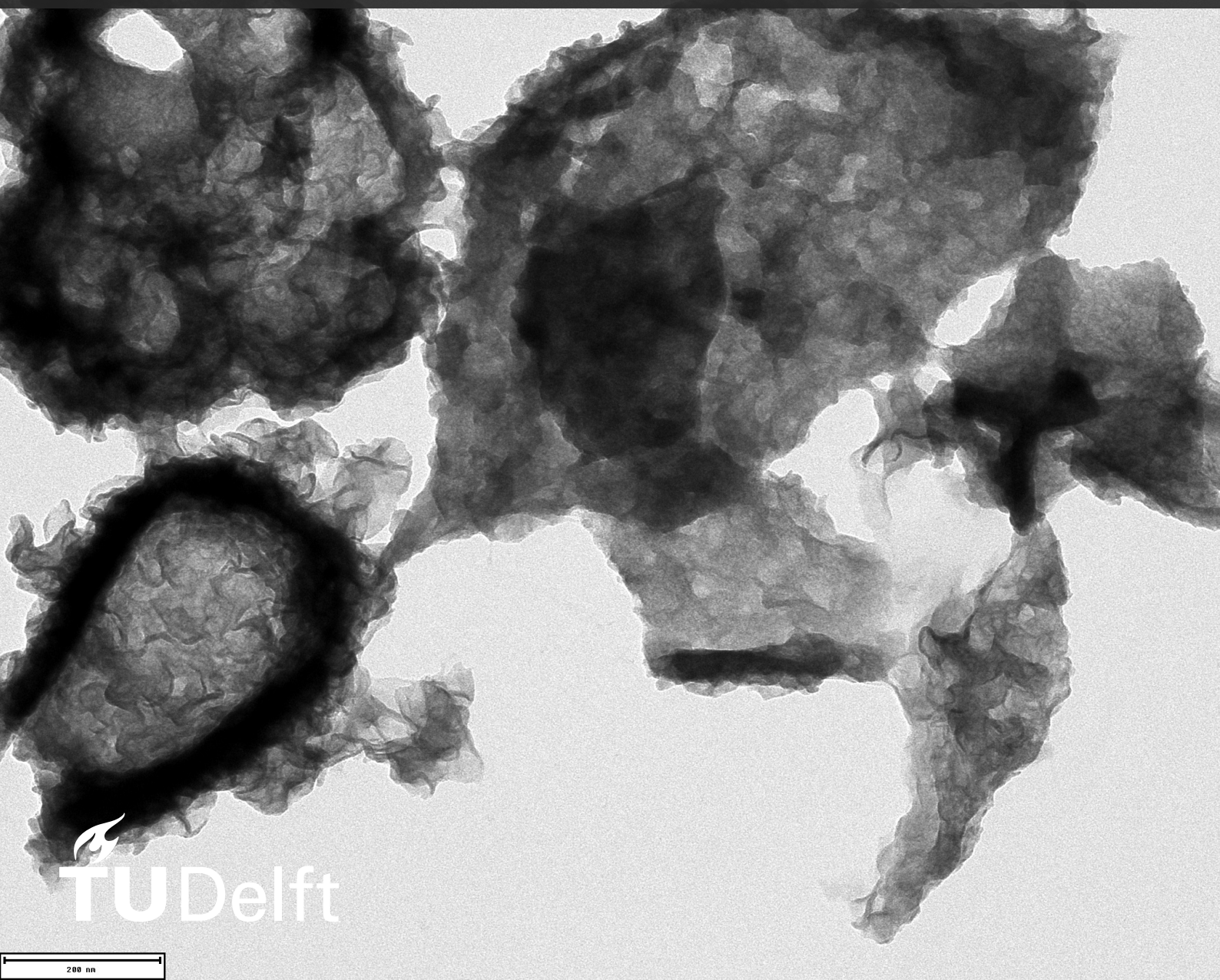

TU Delft

Synthesis, stability tests and irradiation evaluation of hollow MoS_2 nanomaterials

With applications in a new circular low-activity technetium-99m generator

by

Caro van Dijk

Student Name	Student Number
Caro van Dijk	5295092

Supervisor:	Dr. ir. Robin de Kruijff
Daily Supervisor:	Gauri
Project Duration:	February, 2024 - June, 2024
Faculty:	Faculty of Applied Sciences, Delft

Cover: TEM image of MoS_2 nanostructure (synthesized in this report).

TU Delft

Preface

Before you lies the bachelor thesis *synthesis, stability tests and irradiation evaluation of hollow MoS_2 nanomaterials*. This thesis has been written to meet the requirements for completing the bachelor Nanobiology at Delft University of Technology and Erasmus MC. The research reported in this thesis has been carried out between February and May of 2024.

This study builds on research done in the Applied Radiation and Isotopes department in the Reactor Institute Delft, which aims to find a design for a new circular low-specificity $^{99}Mo/^{99m}Tc$ generator.

I would like to thank my supervisors dr. ir. Robin de Kruijff and Gauri for all the guidance and support during this project. I would also like to thank all the technicians, students, phd'ers and all other staff in the ARI group and in the RID for the support and comfort during the project.

I hope you enjoy reading.

Caro van Dijk
Delft, June 2024

Abstract

Technetium-99m (^{99m}Tc) is a critical isotope in nuclear medicine, used for diagnostic imaging. It is conventionally produced in a aluminum oxide ^{99}Mo/^{99m}Tc generator that runs on molybdenum-99 (^{99}Mo) produced by fission of uranium-235. This fission-based production method faces several challenges. To address these challenges, alternative production pathways are being explored. Neutron irradiation of enriched ^{98}Mo nanomaterials and proton bombardement of enriched ^{100}Mo nanomaterials are two of the possible options. Within this research, the pathway of ^{98}Mo neutron capture will be the focus. Developing a novel circular low specific activity ^{99}Mo/^{99m}Tc generator that can run on these materials requires research to be done into the potential materials. The materials must meet two qualifying conditions: they should have a high surface-to-volume ratio, and show high radionuclide extraction potentials. This is an exploratory study to determine if molybdenum disulfides can be synthesized to meet those conditions. Multiple synthesis methods of MoS_2 nanostructures were explored, and insights were given on their morphological and compositional characteristics. Of the six synthesized materials, four were MoS_2 nanospheres, one was MoS_2 microcubes and one was unable to be characterized due to unsuccessful separation of the product. Two of the products were further evaluated on their stability and surface area. Stability tests in milliQ were done under two conditions: five consecutive cycle washes and five time-based washing cycles. Both materials exhibited lower Mo breakthrough during the consecutive washes than during the time-based wash cycles. The most compelling results were the downward trend that the Mo breakthrough data shows for the consecutive washes and the high breakthrough percentage in the 24 h soak for one of the samples (namely, $1.2 \pm 0.28\%$) . Furthermore, the same two materials were tested on irradiation performance. Radionuclide extractions were made in milliQ, and extraction yields were calculated for ^{99}Mo.

Contents

Preface i

Abstract ii

1 Introduction 1

2 Theory 3
- 2.1 Production of ^{99m}Tc . . . 3
- 2.2 Molybdenum based nanomaterials to generate ^{99m}Tc . . . 4
- 2.3 Analytical Instruments . . . 5
  - 2.3.1 X-ray Diffraction . . . 5
  - 2.3.2 Scanning Electron Microscopy . . . 5
  - 2.3.3 Transmission Electron Miscroscopy . . . 5
  - 2.3.4 Brunauer–Emmett–Teller . . . 6
  - 2.3.5 Germanium Detector . . . 6
  - 2.3.6 Inductively Coupled Plasma Mass Spectrometry . . . 6

3 Materials & Methods 8
- 3.1 Materials . . . 8
- 3.2 Methods . . . 9
  - 3.2.1 Method 1 . . . 9
  - 3.2.2 Method 2 . . . 9
  - 3.2.3 Method 3 . . . 10
  - 3.2.4 Method 4 . . . 10
  - 3.2.5 Method 5 . . . 11
- 3.3 Stability Tests . . . 11
- 3.4 Irradiation . . . 12

4 Results and Discussion 15
- 4.1 Synthesis and Characterization of the Materials . . . 15
  - 4.1.1 Synthesis and Characterization of product **1** . . . 15
  - 4.1.2 Synthesis and Characterization of product **2** . . . 15
  - 4.1.3 Synthesis and Characterization of product **3** . . . 19
  - 4.1.4 Synthesis and Characterization of product **4** . . . 20
  - 4.1.5 Synthesis and Characterization of product **5** . . . 22
- 4.2 Stability . . . 25
- 4.3 ^{99}Mo and ^{99m}Tc extraction . . . 27

5 Conclusion and Recommendations 29

References 32

A Appendix 36

B Images 37

1

Introduction

There are numerous radioactive nuclides that either have been, or potentially could be, employed in nuclear medicine. However, in current nuclear medicine, technetium-99m (^{99m}Tc) is used in about 85-90$\%$ of all examinations where radionuclides are involved [1],[2]. This prominent role of ^{99m}Tc in contemporary nuclear medicine highlights its importance within the field.

In the late 1950s and early 1960s, (^{99m}Tc) first began its uprise in medical practice. ^{99m}Tc was found to be very effective in medical imaging such as SPECT-scans (Single Photon Emission Computed Tomography). ^{99m}Tc is obtained by the natural decay of molybdenum-99 (^{99}Mo) with β^- decay. It has a short half-life of 6 hours, emitting a pure 140 keV gamma ray [3]. Furthermore, ^{99m}Tc emits minimal β radiation, which is non-penetrating through human tissue and can thus cause significant localized damage. These properties of ^{99m}Tc make it very suitable to use in nuclear medicine: it ensures that the total radiation dose to the patient is kept at acceptable levels, while the 140 keV photon is strong enough to penetrate tissue successfully, allowing for the visualization of deep organs [4]. The short half-life of the radionuclide assures that the patient is not exposed to radiation for a long time.
The isotope ^{99m}Tc is used in medical imaging as a radioactive tracer to assess how particular parts of our body are working and functioning. Different labelling kits can be designed in a way to transform $^{99m}TcO_4^-$, the configuration in which ^{99m}Tc is extracted from the current generators, to different chemical forms which make it suitable to target specific organs like the brain, thyroids, heart and much more and processes like blood flow to the heart or spread of cancer to the bones. In Fig 1.1, a SPECT-scan can be seen, made with a ^{99m}Tc-labeled compound called methylenediphosphonate or MDP. This compound is a specific target compound that is taken up in the bone while being eliminated from the rest of the body.

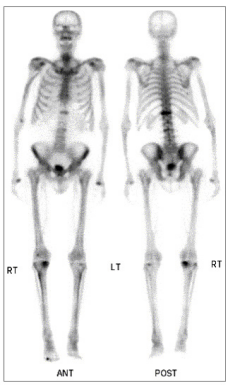

Figure 1.1: A bone SPECT-scan taken with ^{99m}Tc [5].

The most common way to produce ^{99m}Tc is through a ^{99}Mo/^{99m}Tc generator. The present route of production of the ^{99}Mo used in these generators is the fission of uranium-235 (^{235}U), producing fission-

based molybdenum, F^{99}Mo. More than 95% of the F^{99}Mo used for ^{99m}Tc production is produced in a total of seven reactors worldwide . A few other reactors can also produce F^{99}Mo in small amounts, but this is primarily to meet local, and sometimes regional, needs and is not done on a regular basis [6] . Planned and unplanned shutdowns of reactors can easily cause substantial disruptions in the supply of ^{99}Mo, and thus disrupt the production of ^{99m}Tc. Additionally, the ^{235}U utilized for this fission process is under scrutiny. The ^{235}U used for the process used to be Highly Enriched Uranium (HEU, >20% ^{235}U). However, because of concerns regarding nuclear proliferation associated with HEU, the use of HEU targets is being phased out. Five out of the seven reactors have already shifted to Low Enriched Uranium (LEU, generally 3-5% ^{235}U, max 20%) as the ^{235}U source, and the remaining two are planning a switch in the near future. While this shift is beneficial in terms of reducing nuclear proliferation risks, since LEU cannot be fashioned into nuclear weapons without further enrichment, it does have a negative effect on the efficiency of the fission process of ^{99}Mo. Assuming the same uranium target design and uranium density, the yield when using LEU is only about 20-50% of HEU. Additionally, the radioactive waste production increases by 200% [7]. This lower yield and higher radioactive waste are mainly due to the reduced ^{235}U mass in LEU and its increased neutron capture. Since LEU contains a higher mass percentage of other uranium isotopes than ^{253}U compared to HEU, these other isotopes, primarily ^{238}U, will cause more neutron capture, thereby lowering the neutrons available for ionization of target materials [8].
Additionally, although use of LEU makes nuclear weapon manufacture more complicated, it still relies on the same enrichment technologies, albeit on a smaller scale. As long as these technologies are researched, improved and used, the danger of nuclear proliferation remains.

These problems in reliability of supply, proliferation risk and radioactive waste undermine the trustworthiness of this production route. Considering the current demand for ^{99m}Tc is observed to grow around $3-5\%$ anually [9], ensuring a constant and reliable supply of ^{99m}Tc is vital for delivering the diagnostic advantages of ^{99m}Tc-based imaging. Alternative production pathways are already described in literature [10],[11],[12]. Cyclotron production of ^{99m}Tc is one alternative production route being researched. This production route does not involve fission of uranium. By proton bombardment of highly enriched ^{100}Mo (>99.5% ^{100}Mo), ^{99m}Tc is directly formed. This high percentage of enrichment is needed because otherwise the radioactive impurities would be too high for medical use. The nuclear reaction happening is denoted as ^{100}Mo(p,$2n$)^{99m}Tc. This describes the nuclear reaction in which ^{100}Mo is bombarded with a proton, resulting in the production of two neutrons and decay product ^{99m}Tc. However, a drawback to this method is the significant co-production of ^{99g}Tc, a long-lived impurity [13]. In literature, the direct formation of ^{99g}Tc in cyclotron production is model calculated to be 3 to 4 times higher than the direct formation of ^{99m}Tc [12],[13]. This needs further attention and careful consideration before implementing such a production route.
Another alternative production route is making use of the neutron capture reaction of ^{98}Mo, denoted by ^{98}Mo(n,γ)^{99}Mo. Neutrons are captured by ^{98}Mo, resulting in a photon and ^{99}Mo. This reaction can form a new ^{99}Mo source, allowing a step away from fission-based ^{99}Mo. However, this method also has its problems: the probability of ^{98}Mo neutron capture is very low compared to ^{235}U fission, resulting in a production rate that is about 250 times lower and in a low specific activity (defined as the radioactivity per unit mass) ^{99}Mo product [12]. This is, however, a fixable problem. A new design for ^{99}Mo/^{99m}Tc generators, making use of enriched ^{98}Mo-based nanomaterials with a high surface-to-volume ratio and a stable structure could be a potential solution. The objective of this study is to investigate hollow molybdenum sulphides reported in literature so far, and analyse the stability of such materials from an application perspective towards a new ^{99}Mo/^{99m}Tc generator.

2

Theory

2.1. Production of ^{99m}Tc

^{99}Mo and ^{99m}Tc have a mother-daughter relationship. The decay of ^{99}Mo, as the mother nuclide, results in the daughter nuclide ^{99m}Tc. The decay of the mother nuclide increases the number of daughter atoms [14]. Thus, production and disintegration of the daughter nuclide happen simultaneously. After six half-lives of ^{99m}Tc, the nuclides are said to be in equilibrium. The half life of ^{99}Mo is bigger than the half life of ^{99m}Tc, allowing them to grow into an equilibrium. The half-life of ^{99m}Tc is, however, not negligible compared to the half life of ^{99}Mo, making the specific equilibrium for ^{99}Mo and ^{99m}Tc a transient equilibrium [14]. Molybdenum has an atomic number of 42 and is classified as a transition metal. It is naturally occurring in the earth's crust at about 1.5 ppm (part per million) and in the ocean at about 10 ppm. The seven naturally occurring stable isotopes, with their natural abundance percentage, are ^{92}Mo (14.84%), ^{94}Mo (9.25%), ^{95}Mo (15.92%), ^{96}Mo (16.68%), ^{97}Mo (9.55%). ^{98}Mo (24.13%) and ^{100}Mo (9.63%) [15].
The most exploited current production route of ^{99m}Tc is with the ^{99}Mo/^{99m}Tc generator. This generator system is based on the principle that the shorter-lived radioactive daughter nuclide ^{99m}Tc can be easily and repeatedly isolated from its longer-lived parent nuclide ^{99}Mo. The ^{99}Mo used in the current generators is produced by the fission of HEU or LEU. The ^{99}Mo obtained from fission is called F^{99}Mo. This F^{99}Mo decays naturally to ^{99m}Tc with a half-life of 65.9 hours. The decay scheme of ^{99}Mo can be seen below in 2.1.

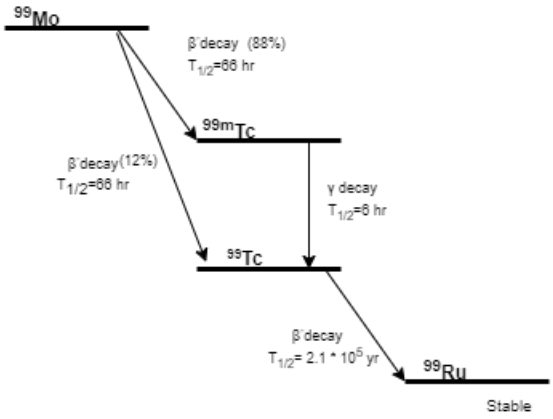

Figure 2.1: Decay scheme of ^{99}Mo, created with draw.io [16].

The generators contain aluminum oxide (Al_2O_3) loaded in a plastic or glass chromatographic column situated in a lead container. ^{99}Mo is bound to the aluminum in the form of MoO_4^{2-}, which decays to pertechnetate, $^{99m}TcO_4^-$. Because of the single charge of pertechnetate, it has less affinity for the

column and is thus bound less tightly than MoO_4^{2-}. Flushing the column with a saline solution (0.9% NaCl) elutes the soluble ^{99m}Tc, isolating it free of contamination from the parent nuclide ^{99}Mo [17]. After flushing, the ^{99m}Tc concentration is largely depleted from the column. This immediately starts to increase again due to the continuing decay of ^{99}Mo, as seen in Fig 2.2. In hospitals, ^{99}Mo/^{99m}Tc generators are usually eluted after 24 h, 4 times the half life of ^{99m}Tc. Note that the extraction is made two half lives before the generator reaches transient equilibrium. This is done to optimize the activity yield of ^{99m}Tc.

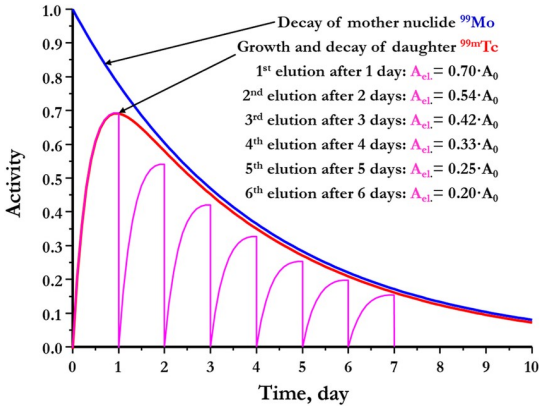

Figure 2.2: ^{99}Mo and ^{99m}Tc generator extraction system [18].

The clinically useful lifetime of such a fission-based ^{99}Mo/^{99m}Tc generator is generally 2 weeks. These generators are used locally in the hospitals. This production route thus avoids the problems of the fast decay of ^{99m}Tc and the necessity for rapid delivery of ^{99m}Tc to the sites where it is being used [17] [19].

This is the method most commonly used for production of ^{99m}Tc since 1958 [3]. With F^{99}Mo being widely and readily available worldwide along with the advanced alumina column generator technology, there was no need to search for new alternative production routes of ^{99m}Tc. However, after 2007 a variety of factors resulted in the reduced availability of the alumina based ^{99}Mo/^{99m}Tc generators worldwide. The supply of ^{99m}Tc was cut by 20-70% in 2007, mainly caused by repeated temporary shutdowns for age-related maintenance of two out of seven reactors producing ^{99}Mo. The crisis period is now over, but this supply shortage alerted many about the vulnerability of the current production route of the ^{99}Mo needed for the production of ^{99m}Tc, and justly so [9]. The goal to reduce the use of HEU and switch to LEU, bringing with it some complications to the process, combined with the unreliable workings of the few ageing reactors worldwide for the production of F^{99}Mo triggered the search for an alternative source of ^{99m}Tc, reducing the need for the alumina based ^{99}Mo/^{99m}Tc generator with F^{99}Mo as molybdenum source [20].

2.2. Molybdenum based nanomaterials to generate ^{99m}Tc

^{98}Mo or ^{100}Mo based nanomaterials can be used to produce ^{99}Mo. This route of production poses a few obstacles upon initial assessment, which will be more widely discussed in this section: when making ^{99}Mo from fission of ^{235}U, this produces a high specific activity of ^{99}Mo. In comparison, producing ^{99}Mo from ^{98}Mo and ^{100}Mo, gives a significant decrease in specific activity, namely 4-5 orders of magnitude lower than ^{99}Mo obtained from ^{235}U fission. Enriching the ^{98}Mo target can increase the specific activity of the produced ^{99}Mo by a factor of four (^{98}Mo enrichment of $\geq$96%) [18]. This already helps a lot, but it is still significantly lower than the specific activity produced with fission. With the high-specific F^{99}Mo and the current alumina column technology, an aluminum column of about 2-5 grams is used [21]. With the enriched ^{98}Mo route, a large alumina column of about 60 grams would be needed. This large column then requires a large eluent volume of saline solution to elute ^{99m}Tc. The large eluent volume results in a low radioactive concentration of TcO_4^-, which makes the extraction liquid unsuitable for medicinal applications [21]. Thus, another way of producing, separating and collecting the ^{99m}Tc should be investigated.

There has been a growing interest in nanomaterials and their properties in recent years. Certain proper-

ties which are unique to nanomaterials can provide substaintial benefits in the extraction of ^{99m}Tc. Many of these properties arise from the large surface-to-volume ratio of nanomaterials. Some of these properties are improved surface reactivity due to the large surface area and improved radiation resistance compared to bulk materials [22].

Consequently, nanomaterials could be a promising candidate for a new ^{99}Mo/^{99m}Tc generator. This requires further research on the possible synthesis and separation techniques. Currently, there is a lot of research on the potential role of MoS_2 hollow nanoparticles in energy storage, for example in supercapacitors or lithium-Ion batteries [23],[24],[25],[26],[27]. MoS_2 has unique physical and chemical properties that make it a suitable candidate in energy storage applications. The focus of this report is on the synthesis of hollow MoS_2 with a high surface area, suitable for irradiation and extraction of ^{99m}Tc. Notably, Mo was first discovered in the form of MoS_2, by Swedish chemist Carl Wilhelm Scheele [15]. MoS_2 nanomaterials are seen in literature to be of hydrophobic nature [28]. This makes molybdenum sulfides a good subject for ^{99m}Tc extraction with milliQ as medium, since minimal amount of molybdenum will be flushed out with the technetium. In a solution of milliQ and MoS_2, the decay product ^{99m}Tc will most likely be present in the configuration TcO_4^-, pertechnetate. This is a polar, hydrophilic substance, which will be easily flushed out by a milliQ wash. Since the current generators also produce TcO_4^- as the extracted form of ^{99m}Tc, labelling kits are already designed to transform TcO_4^- to the needed chemical forms of ^{99m}Tc.

2.3. Analytical Instruments

2.3.1. X-ray Diffraction

X-ray diffraction analysis makes use of Bragg's Law:

$$n\lambda = 2dsin(\theta) \tag{2.1}$$

Where n is an integer representing the diffraction order, λ is the wavelength of the X-ray photons in meters, d_{hkl} is the interplanar distance in the crystal lattice in meters and θ is the Bragg's angle in degrees. In an XRD measurement the X-rays are reflected off the atoms and thus the reflected intensities give information about the periodicity of the atom structure. By observing the angles at which reflection of a monochromatic X-ray beam takes place, information about the crystal structure can be obtained. [29]

2.3.2. Scanning Electron Microscopy

Scanning Electron Microscopy (SEM) is a technique that uses electrons to image objects at a very high image resolution compared to light microscopy. Imaging with electrons allows for interaction between the negatively charged electron and the atoms to be imaged. The magnifying range for SEM is about 10–500,000 times. However, a disadvantage of electron microscopy is that the sample need to be imaged in a vacuum, otherwise the electrons get scattered due to their interactions with the air. This requirement for a vacuum environment can be in conflict with the nature of the material to be imaged. In SEM, the electron beam is focused on one spot and moves successively across the sample. The sample emits signals at each location, which are collected by the detectors. The detector signal is synchronized with the known location of the beam on the sample. The signal intensity is then used to modulate the corresponding image pixel. The dimensions and pixel distribution of the image are dependant on the selected scan pattern. Typical electron energies are 1-30 keV [30]. A schematic overview of a SEM is shown in Fig 2.3a.

2.3.3. Transmission Electron Miscroscopy

In Transmission Electron Microscopy (TEM), all the concepts mentioned above for electron microscopy hold true. The magnification range of TEM is 2000 to 1 million times. This high magnification range allows for characterization of microstructures and nanostructures at many different length scales within one imaging session. In TEM the electron beam, also referred to as "electron gun", is directed onto a defined area of the sample. To form an image, electrons that are transmitted through the sample are focused by lenses and captured by a parallel detector. Electron energies in TEM are usually 80-300 keV. These are relatively high energies, needed to enable the electrons to pass through the sample [30]. A schematic overview of a TEM is shown in Fig 2.3b.

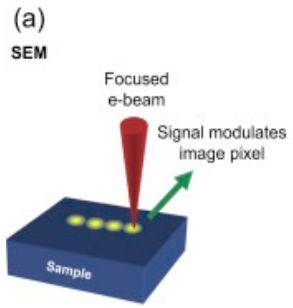

(a) Image acquisition in SEM (retreived from [30]).

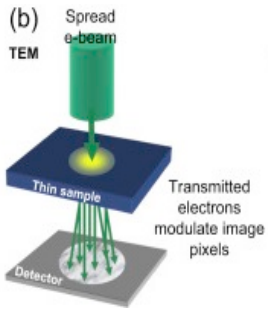

(b) Image acquisition in TEM (retreived from [30]).

Figure 2.3: Image acquisition in Electron Microscopy methods.

2.3.4. Brunauer–Emmett–Teller

The Brunauer–Emmett–Teller (BET) surface adsorption method is a method used to measure the surface area of nanoparticles. The analysis is named after the three authors of a paper from 1938 describing the theory behind the analysis. The BET equation used for gas adsorption is as follows:

$$v = \frac{v_m cp}{(p_0 - p)[1 + (c-1)(\frac{p}{p_0}])} \tag{2.2}$$

Where v is the adsorbed volume of gas in mL or cm^3, v_m is the adsorbed monolayer volume in mL or cm^3, p is the equilibrium gas pressure in Pa, p_0 is the saturation pressure in Pa and c is the BET constant, which is dimensionless. A probing gas, called the adsorbate, that does not react chemically with the material to be analyzed, called the adsorptive, is needed to quantify specific surface area. In the uses in this report, nitrogen gas is used as the adsorbate. The BET theory takes a number of assumptions: it assumes a homogeneous surface, meaning adsorption occurs equally across the entire surface. It also assumes limited molecular interactions, local equilibrium (rate of adsorption is equal to the rate of desorption), a kinetically limited process (energy must be provided in the form of heat for the reaction to proceed) and infinite adsorption at saturation (once p_0 is reached, the material is assumed to be saturated completely)[31].

2.3.5. Germanium Detector

Germanium detectors are γ-ray detectors. The Ge-detector used in this report is an intrinsic germanium detector, also called a high-purity germanium. Germanium is a semiconductor material. Semiconductors have proven to have the best energy resolution from radiation spectrometers in everyday use. Electron-hole pairs act as the information carriers. The electron-hole pair is created in the wake of a charged particle, i.e. primary radiation or secondary particles, and the flow of these electrons-hole pairs in an applied electric field generated the electrical signal from the detector. In ultra-pure germanium, impurity levels as low as 10^9 atoms/cm^3 are achieved. The detector is cooled with liquid nitrogen to a temperature of 77 Kelvin. This is done to reduce the leakage current to the point where the associated noise does not lower the energy resolution significantly.
The detector itself must be placed in a vacuum-tight cryostat in order to prevent heat conduction between the crystal and the surrounding air. This is required because heat conduction can lead to random generation of electron-hole pairs without radiation interaction, resulting in false counts [32].

2.3.6. Inductively Coupled Plasma Mass Spectrometry

Inductively Coupled Plasma Mass Spectrometry (ICP-MS) is a technique that can determine low concentrations of elements in a solution, in the range of parts per billion (ppb, μg/L) or even parts per trillion (ppt, ng/L). The sample that is to be measured has to be diluted with HNO_3, with a concentration between 1% and 10% to make it compatible with the ICP-MS system. The samples are converted into a fine aerosol and transported to a plasma source, where they become ionised. The ions are channeled into a mass spectrometer. The mass spectrometer can only measure one mass-to-charge ratio at a time, meaning that only one element can be measured at a time. Ions with another mass-to-charge

ratio will not be allowed to pass through the mass spectrometer. As they leave the mass spectrometer, ions hit an electron multiplier, which serves as a detector. The following cascade of electrons is amplified until it becomes a measurable pulse, which is then related to the standard intensities in the software (the calibration curve) to determine to concentration of the element [33].

3

Materials & Methods

3.1. Materials

Chemical Name	**Chemical Formula**	**Supplier**
Sodium Molybdate	Na_2MoO_4	Thermoscientific
Thioacetamide	C_2H_5NS	Thermoscientific
Molybdenum Trioxide	MoO_3	Alfa Aesar
Sodium Fluoride	NaF	Sigma Aldrich
Potassium Thiocynate	KSCN	Merck
Thiourea	$CS(NH_2)_2$	Sigma Aldrich
1-Butyl-3-methylimidazolium chloride (Ionic Liquid)	[BMIM]Cl	Merck Sigma
Molybdyl Acetoacetonate	$C_{10}H_{14}MoO_6$	Sigma Aldrich
Manganese(II)chloride tetrahydate	$MnCl_2{\cdot}H_2O$	Merck
Sodium Carbonate	Na_2CO_3	Baker Analyzed
L-cysteine	$C_3H_7NO_2S$	Merck
Manganese(II)sulfate	$MnSO_4{\cdot}H_2O$	Merck
Ammonium Sulfate	$(NH_4)_2SO_4$	Merck Millipore
Ammonium Bicarbonate	NH_4HCO_3	Baker Analyzed
MilliQ	H_2O	Ultrapure water system, Advantage A10, Merck
Isopropanol	C_3H_8O	VWR Chemicals
Ethanol	C_2H_6O	VWR Chemicals
Hydrochloric Acid	HCl	Supelco
Nitric Acid	HNO_3	Honeywell
Sulfuric Acid	H_2SO_4	Sigma Aldrich

Table 3.1: Materials used.

3.2. Methods

All methods are based on hydrothermal synthesis in a Teflon-lined stainless steel autoclave, as is depicted in Fig 3.1 below.

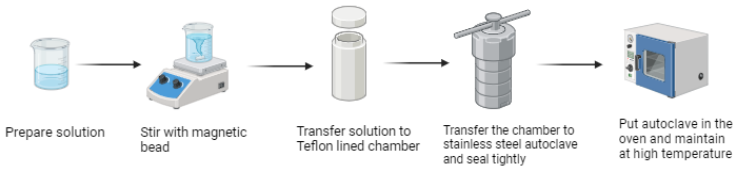

Figure 3.1: The hydrothermal synthesis method. Created with BioRender [34].

The structural details of the materials synthesized were studied with XRD patterns on PW0304 X'Pert PRO, Philips, with a Cu-K_α radiation (λ = 0.15 nm) source. The instrument was operated at voltage of 40 kV and a current of 40 mA, a scanning region of $2\theta = 5 - 90°$. The patterns were analysed using Highscore Plus software and Origin Pro 2024, and compared to those present in the literature.

The morphology and particle sizes of the materials were imaged using electron microscopy. ISM-IT100 InTouchScope SEM, JEOL was used at 10-20 keV acceleration voltage. The elemental composition and purity of the materials were qualitatively determined by Energy Dispersive X-ray (EDX) analysis through detectors attached to the SEM.
TEM was conducted on a JEM-1400 Plus TEM, JEOL at an acceleration voltage of 120 keV. The images obtained by SEM and TEM were analysed using ImageJ [1].

3.2.1. Method 1

In a typical synthesis, 0.120 g of sodium molybdate (Na_2MoO_4) and 0.240 g of thioacetamide (C_2H_5NS) were dissolved in 80 mL of milliQ water with continuous stirring [23]. The mixture was left on the magnetic stirrer for 10 min. The as-obtained mixture was then transferred into a 100 mL Teflon-lined stainless steel autoclave and heated at 200 °C for 24 hours. After heating, the autoclave was cooled to room temperature naturally. The sample was filtered in two different ways, namely by Büchner funnel and by centrifuging at 9500 rpm. No precipitates were obtained by filtering with a Büchner funnel nor by centrifuging in a 50 mL tube and 15 mL tube for 5 min. The 15 mL tube was placed in the oven at 60 °C for two days, after which it was taken out and allowed to settle down naturally for seven days. The 50 mL tube was allowed to settle down naturally for 25 days. A few more centrifugal methods were tried: two 2 mL aliquots were centrifuged at 13,000 rpm for 10 min; a mixture of 1 mL reaction mixture and 1 mL ethanol was centrifuged at 13,000 rpm for 10 min; the 15 mL tube was centrifuged at 9500 rpm for 10 min after seven days of settling down; the 50 mL tube was centrifuged at 9500 rpm for 10 min after 25 days of settling down. The product, henceforth referred to as **1**, was hereafter allowed to settle down naturally in both the 15 mL tube and the 50 mL tube [23].

3.2.2. Method 2

In a typical synthesis, 0.865 g of molybdenum trioxide (MoO_3), 0.515 g of sodium fluoride (NaF) and 1.930 g of potassium thiocyante (KSCN) were added to a mixture of 25 mL milliQ and 10 mL ethanol [24]. After being stirred for 10 min, the solution was then transfered to a 50 mL Teflon-lined stainless steel autoclave and heated at 200 °C for 16 h. The precipitates were then filtered out with a Büchner funnel and washed several times with milliQ, diluted acid (HCl, HNO_3, H_2SO_4) and ethanol. A separate liquid waste disposal was set up in the fume hood during filtration to collect the liquid obtained after the reaction was completed, because of the potential formation of CN^- in the solution.
An acid wash was described in the literature [24] to wash the $K_2NaMoO_3F_3$ core away. Several different acid wash approaches were tried, namely:

- 2 M HCl wash 1: several washes with HCl, then two rounds of 30 min soaking in fresh 2 M HCl, resulting in single acid wash sample;

[1] ImageJ is a free image processing software that can be downloaded from [35].

- 2 M HCl wash 2: sonication of the single acid wash sample for 5 min in 2 M HCl and subsequential soaking in fresh 2 M HCl for 24 h, resulting in double acid was sample;
- 0.5 M HNO_3 acid wash: Three rounds of sonication for 30 min in fresh 0.5 M HNO_3 solution, whereafter the material was allowed to soak in HNO_3 for 18 h.

Finally, the product, henceforth referred to as **2**, was dried at 60 °C under vacuum for 18 h [24].

Synthesis and dissolving of $K_2NaMoO_3F_3$ core

The core was synthesized separately to be able to better determine which acid would dissolve the core most effectively. To be able to synthesize the $K_2NaMoO_3F_3$ core separately, without formation of the MoS_2 shell, another K source had to be added to the solution that did not contain sulfur. To this end, KF was synthesized, as described in detail in Appendix A. With this new K source, the $K_2NaMoO_3F_3$ core could be synthesized individually, as this was also shown in literature [36]. The synthesis described above was repeated, with KF instead of KSCN. The resulting product will henceforth be referred to as the core.
The following experiment was done once with the separately synthesized core. Five concentrations of acids HCl, HNO_3 and H_2SO_4 were subsequently prepared, namely: 0.01 M; 0.1 M; 0.5 M; 1 M and 5 M. 50 mg of the core was added to 15 mL tubes, followed by the addition of 5 mL of the corresponding acid. These 15 tubes then underwent sonication for two min, followed by an additional 30 min of sonication, and were then allowed to settle overnight. Empty tubes were weighed, and the acid solutions were sonicated once more for 10 min before being transferred to the new tubes, which were then centrifuged at 9500 rpm for 5 min. Liquid was pipetted off. The solutions were then placed in the oven at 80 °C under a vacuum of 400 mbar to dry for two days, followed by drying at 90 °C for two more days.

Degradation MoS_2 in acids

The MoS_2 nanomaterial had to be able to withstand the chosen acid during the acid wash. To determine which acid concentration would be most optimal for the experiment, new solutions were prepared by combining 50 mg of previously synthesized MoS_2 with 5 mL of each respective acid and its concentration. Two acid concentrations were chosen for this, namely 0.5 M and 1 M HNO_3. These solutions were used to evaluate the degradation of MoS_2. The solutions were sonicated for 2 min, followed by an additional 30 min of sonication, and were then left overnight. The solutions were then centrifuged at 9500 rpm for 5 min, and the top liquid was pipetted off. They were then placed in the oven at 90 °C for 48 h, followed by a vacuum oven at 80 °C for 4 h. The final product was weighed and compared to the initial weight.

3.2.3. Method 3

In a typical synthesis, 0.72 g of sodium molybdate (Na_2MoO_4) and 0.69 g of thiourea ($CS(NH_2)_2$) were dissolved in V_1 milliQ under stirring [37]. V_2 of ionic liquid [BMIM]Cl (1-butyl-3- methylimidazolium chloride) was added under vigorous stirring. The literature [37] had defined a volume V_1 for milliQ and a volume V_2 for [BMIM]Cl, with the total volume V = V_1 + V_2 = 60 mL. Additionally, the literature's results [37] stated that the optimal volumetric ratio was V_2/V_1 = 1/9. Thus, volumes V_1 = 54 mL and V_2 = 6 mL were used. However, since the [BMIM]Cl was in solid form, the required mass to obtain 6 mL was calculated using $\rho = m/V$, resulting in a mass of 6.5 g. This 6.5 g was dissolved in 30 mL milliQ under stirring. The other reactants were dissolved in the remaning 30 mL milliQ, and added to the 30 mL milliQ/[BMIM]Cl solution under stirring.

Then 30% HCl (9.46 M) was added to the solution under stirring to adjust the pH value to less than 1. The solution was then transferred to a 100 mL Teflon-lined stainless steel autoclave and put in the oven at 180 °C for 24 h. The product, henceforth referred to as **3**, was collected with a Büchner funnel, washed with milliQ seveal times and air dried for four days [37].

3.2.4. Method 4

This synthesis consists of two parts. The first part is synthesizing solid molybdenum-based spheres, then the synthesis of hollow MoS_2 spheres.
In a typical synthesis, a solution **A** was prepared by dissolving 0.23 g of molybdyl acetoacetonate ($C_{10}H_{14}MoO_6$) in 15 mL isopropanol by sonication for 5 min and 15 min, in two different rounds of synthesis. [25]. Then, 20 mL isopropanol and 25 mL milliQ were mixed and added to solution **A** under

magnetic stirring. The reaction mixture was stirred in two different ways in two respective rounds of synthesis: stirring for 5 min; stirring for 16 h. After the 16 h stirring the solution was refilled to 60 mL again with isopropanol to replace the isopropanol that evaporated. The mixture was transferred into a 100 mL Teflon-lined stainless steel autoclave and heated at 190 °C for 3 h, centrifugally separated and washed with ethanol four times before being put in the vacuum oven at 60 °C for 12 h.

Subsequently, starting the second part of the synthesis, 0.06 g of the molybdenum-based solid spheres template was dispersed in a solution containing 24 mL ethanol and 10 mL milliQ, forming solution **B**. After stirring on the magnetic stirrer for 10 min, 0.08 g of thiourea ($CS(NH_2)_2$ was added into solution **B**. The final solution was transferred to a 100 mL Teflon-lined stainless steel autoclave and put in the oven at 180 °C for 12 h. After cooling down to room temperature naturally, the solution was centrifugally filtered and washed with milliQ and ethanol twice, respectively. The product, henceforth referred to as **4**, was then transferred to a vacuum oven where it was kept at 60 °C for 19 h [25].

3.2.5. Method 5

5a

In a typical synthesis of the spheres, 2.6 g of Na_2CO_3 and 4.9 g of $MnCl_2{\cdot}H_2O$ were dispersed in 25 mL milliQ each. Additionally, one round of synthesis was done with half off all the values, The $MnCl_2$ solution was gradually added to the Na_2CO_3 solution under magnetic stirring. Several stirring times were tried, namely t = 15 min and t = 30 min. The reaction mixture was then removed from the magnetic stirrer and filtered with a Büchner funnel. The product was washed with milliQ and ethanol several times before being put in a vacuum oven and kept at 60 °C for 18.5 hours.

To synthesize hierarchical hollow MoS_2 nanospheres, 0.2 g of the synthesized $MnCO_3$ spheres was redispersed in 20 mL milliQ through sonication for 30 minutes. After the sonication, 0.3 g $Na_2MoO_4{\cdot}2H_2O$ and 1.25 g $C_3H_7NO_2S$ (L-cysteine) were added, after which the solution was sonicated for another 30 min. Then the solution was transferred into a 50 mL Teflon-lined stainless steel autoclave and kept at 220 °C for 24 h. After cooling to room temperature naturally, the black precipitates were collected centrifugally and washed thoroughly with 10 mL of 1.0 M HCl. The samples in HCl were sonicated for 30 minutes and centrifugally separated. Washing with HCl was repeated 3 times, after which the sample was washed four times with milliQ until the solution became neutral (pH $\approx$ 7). The product, henceforth referred to as **5a** was centrifugally filtered again and dried at 80 °C for 15 h under vacuum [26].

5b

In a typical synthesis of the cubes, 1.51 g of $MnSO_4{\cdot}H_2O$, 13.2 g of $(NH_4)_2SO_4$ and 70 mL ethanol were dissolved in 700 mL milliQ [27]. Next, a second solution was made by dissolving 7.9 g of NH_4HCO_3 in 700 mL milliQ. The second solution was added into the first solution under vigorous stirring. The mixed solution was heated in a water bath and maintained at 50 °C. Two heating periods were tried in two different synthesis rounds, namely: 16 h homogeneous heating; 2 h homogeneous heating with manual stirring every 20 min. The white precipitates were filtered out with a Büchner funnel and put in the oven at 60 °C for 12 h.

To synthesize hierarchical hollow MoS_2 microcubes, 0.4 g of the previously synthesized $MnCO_3$ microcubes was redispersed into 40 mL milliQ by sonication for 60 min. 0.6 g of $Na_2MoO_4{\cdot}2H_2O$ was added to the solution, which was then sonicated for another 10 min before adding 2.5 g of $C_3H_7NO_2S$ and sonicating for another 10 min. The mixture was then transferred to a 50 mL Teflon-lined stainless steel autoclave and maintained at 220 °C for 24 h. The black precipitates where filtered out centrifugally, washed several times with ethanol and put in the oven to dry at 60 °C for 24 h. The dried sample was subsequently washed thoroughly with 10 mL 1.0 M HCl. The samples in HCl were sonicated for 30 min and centrifugally separated. Washing with HCl was repeated three times, after which it was washed four times with milliQ until the solution became neutral (pH $\approx$ 7). Then the product, henceforth referred to as **5b**, was dried in a vacuum oven at 80 °C for 15 h [27].

3.3. Stability Tests

The stability of the molybdenum sulfides was tested in milliQ and measured with ICP-MS. All the experiments were done in triplicate. To calculate the Mo breakthrough in the material, ICP-MS was done

on NexION 2000 ICP-MS, Perikin Elmer.

Typically, 10 mg of **2** and **5a** was dispersed in 500 μL milliQ and sonicated for 30 min. The solution was then passed through a polyethersulfone (PES) membrane centrifugal filter, which was followed up by nine consecutive washes with 500 μL of fresh milliQ. The 10 washes were diluted with 0.22 M HNO_3 (50 μL of the wash and 4.950 mL of 0.22 M HNO_3). The diluted samples were then measured with the ICP-MS to measure the breakthrough of Mo.

Furthermore, 500 μL was again added to the PES membrane and the sample was centrifuged and collected at time t = 0. Then, 500 μL of fresh milliQ was allowed to interact with the material for 30 minutes, before centrifuging collecting the filtrate at time t = 30 min. This was repeated at t = 1 h, 2 h, 16 h and 24 h. The washes were diluted with 0.22 M HNO_3 (0.22 M) using the same ratio as mentioned above, and then measured with the ICP-MS. After air drying for seven days, SEM was used to check any morphological change.

3.4. Irradiation

The irradiations reported here were performed in the BP_3 pneumatic irradiation facility at the Reactor Institute Delft. Typically, 30 mg of the molybdenum material was sealed in a polyethylene (PE) capsule and irradiated for 10 h. The estimated neutron fluxes in the BP_3 facility are: $\Phi_{th} = 4.7 \times 10^{16} m^{-2} s^{-1}; \Phi_{epi} = 8.8 \times 10^{14} m^{-2} s^{-1}; \Phi_{fast} = 3.5 \times 10^{15} m^{-2} s^{-1}$. However, note that these are the neutron fluxes when the facility is operating at 100% power. During the irradiations, the facility was operating at $\sim$60% power, so the neutron fluxes are estimated to be lower. After irradiation, the samples were left to cool down for several hours to allow for decay of the short-lived radionuclides (namely, ^{101}Mo and ^{101}Tc).
The PE capsules containing the irradiated materials were partially opened and transferred into 5 mL glass vials containing 4.5 mL milliQ. The vials were placed in an ultrasonic bath for 30 min to disperse the material. The samples were then magnetically stirred continuously for 30 min before dividing the 4.5 mL solution into three eppendorfs, each eppendorf containing 1.5 mL. The rest of the experiments were done with the assumption that the three aliquots were equally divided, with each eppendorf containing 10 mg of irradiated sample. Hereafter, the experiments were done in triplicate, unless mentioned otherwise.

The eppendorfs were sonicated for 30 min and thereafter centrifuged at 10,000 rpm and 12,000 rpm for 2 min, respectively. Five washes with milliQ were done. Of the five washes, the first was done centrifugally. After the first wash, the 1.5 mL solutions were transferred to a 500 μL PES filter tube, by pipetting 500 μL out three times, pipetting up and down a few times each transfer to facilitate dispersion and complete transfer. After the transfer, the samples were washed four more times to remove any loose material. Between each wash, the samples were centrifuged at 10,000 rpm for 10 min, and all washings were collected. The first and second was were measured in the Ge-detector, from the third wash onward the washes were not measured anymore. Measurements were not necessary because the washes were primarily done to get rid of any excess loose or recoiled $^{98/99}$Mo and perhaps some loose ^{99m}Tc. Following the washes, two extractions per day were performed over a period of five days. The extractions were done at the same time each day. The samples were centrifuged at 11,000 rpm for 10 min, and the extraction liquid was transferred to an eppendorf. After the first two extractions, fresh 500 μL milliQ was placed on top of the sample after each extraction. This was done to loosen up the material, to make the milliQ go through easier. In total, 11 extractions were done. Two per day over the course of five days, and one extra extraction, **K**, to test the differences in measurements depending on the geometries.

To measure counts and calculate extraction yield of the irradiated materials, (HPGe) detector (Princeton Gamma Tech model LG22) Ge-detector was used. The measurements were taken with a measurement time of 120 seconds and analysed with Genie 2000 software. In this software, certain regions of interest (ROI's) can be selected on the x-axis. The measuring height was 18 cm. The sample was measured in a glass vial, pearched on top of three plastic holders with a perspex cilinder around it, to minimize β-radiation exposure. The set up was surrounded by 6 lead rings, to minimize total radiation exposure. The setup can be seen in Fig 3.2. The measuring height of 18 cm was necessary to keep the dead time of the measurements under 5%. The ROI for ^{99}Mo was defined as 726.4-748.5 keV and the ROI for

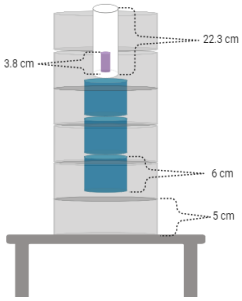

Figure 3.2: Measurement setup for the Ge-detector. Created with Biorender [34].

^{99m}Tc was defined as 135.6-145.7 keV. The Ge-detector measured the activity of the sample in counts, over a measurement time of two minutes, resulting in counts per two minutes as measurements unit. This will be referred to as the activity. Radioactive decay is a random process, governed by statistical laws, derived and explained in [38]. To try to obtain statistically robust results, the measurements were done in triplicate. By doing so, the standard deviation can be calculated for each measurement, quantifying the spread of fluctuations around the mean.

At each extraction, three measurements were taken, see Fig 3.3. Measurement I, **AC**, was done right after centrifugation. Measurement II, **S**, was taken of the solid material left on the filter. Measurement III, **L**, was taken of the liquid extraction. All of the measurements were taken within a maximal time span of an hour. For extractions **A** through **I**, measurements I, II and III were taken. Furthermore, for extractions **J** and **K**, measurement IV was also taken, to try and deduce the role of geometry in the measurement data. For extractions **G** and **I**, an extra measurement was also taken at radioactive equilibrium. This measurement had to be taken after at least six half lives of ^{99m}Tc from the time of centrifuging, to ensure the two radionuclides had reached a radioactive equilibrium. The measurement was taken 4 days after centrifuging for **I** and 6 days after centrifuging for **G**.

Figure 3.3: Measurements geometries. Created with Biorender, [34].

Decay correction for ^{99}Mo was done according to the formula:

$$A(t) = A(0) \times e^{-\lambda t} \tag{3.1}$$

where $A(t)$ is the measured value in cpm, which was corrected back to the time of centrifuging, i.e. disturbing the equilibrium, $A(0)$, λ is the decay constant in s^{-1} and t is time in seconds. For ^{99m}Tc, mother-daughter decay correction needs to be done from an equilibrium measurement, according to the formula for transient equilibria:

$$N_2 = \frac{\lambda_1}{\lambda_2 - \lambda_1} N_1 (1 - e^{(\lambda_1 - \lambda_2)t}) + N_2^0 e^{\lambda_2 t} \tag{3.2}$$

where subscripts 1 and 2 refer to ^{99}Mo and ^{99m}Tc respectively, N_x is the counts of nuclide *x*, N_x^0 is the counts present at time zero for nuclide *x*, λ_x is the decay constant for nuclide *x* in s^{-1} and t is the time in seconds.

4

Results and Discussion

4.1. Synthesis and Characterization of the Materials

4.1.1. Synthesis and Characterization of product 1

Synthesis of the material was done as described in 3.2.1. Separation of the product was not successful. In both the 15 mL tube and the 50 mL tube, the reaction mixture showed quite a lot of solid-like structures accumulated in the solution. However, centrifugation of the tubes resulted in complete dispersion of the product.

The solids that formed were most likely formed through nucleation processes and an Ostwald ripening process, as also mentioned in the literature [23]. Ostwald ripening is a phenomenon observed in liquid solutions that involves a change of an inhomogeneous structure over time. It states that small crystals or solid particles first dissolve in a solution, to subsequently redeposit themselves onto larger crystals or larger solid particles [39]. Following this process, the nanostructures formed themselves in an ensemble of particles, hereby forming larger structures over time that could be observed after a few days. Moreover, weak Van der Waals forces between the particles attract one another to form a larger structure [23]. These forces mainly arise due to temporary dipoles generated by the movement of electrons, leading to the weak attractions between the MoS_2 layers. Additionally, MoS_2 has hydrophobic surfaces that will make the particles aggregate due to the hydrophobic effect [28]. A reason that the formed solids fall apart and completely disperse again during centrifugation, could be that the weak Van der Waals forces cannot withstand the centrifugal forces and the structures fall apart. It is probable that some kind of MoS_2 nanomaterial formed in this synthesis, maybe even nanoporous material, but separation was not successful and thus no characterization could be done.

No further alternative separation methods were done on **1**.

4.1.2. Synthesis and Characterization of product 2

Synthesis of the material was done as described in 3.2.2. The total yield was 406 mg. Since no specific acid was suggested in the literature [24], it was decided to start with 2 M HCl to wash the core away. Single and double 2 M HCl acid wash products were obtained. The single acid wash and double acid wash sample were both characterized using XRD, of which the patterns are displayed in Fig. 4.1a. The double acid wash did contribute to a relatively more crystalline structure; the peaks in the XRD pattern are more defined. However, TEM images showed that the 2 M HCl was not effective in washing away the core. A solid core remained in parts of the product, as can be seen in Appendix B. Therefore, further investigation was necessary to identify the optimal acid and optimal concentration for dissolving the core.

The separate synthesis of the core is described in 3.2.2. The core would be used to determine which acid dissolved the core most effectively. From the XRD pattern of the core, as seen in Fig 4.1b, it can be concluded by comparison to the supporting information from [36] that the synthesis of the $K_2NaMoO_3F_3$ core was successful, with a yield of 860 mg. The acid solutions were made to dissolve the core. After

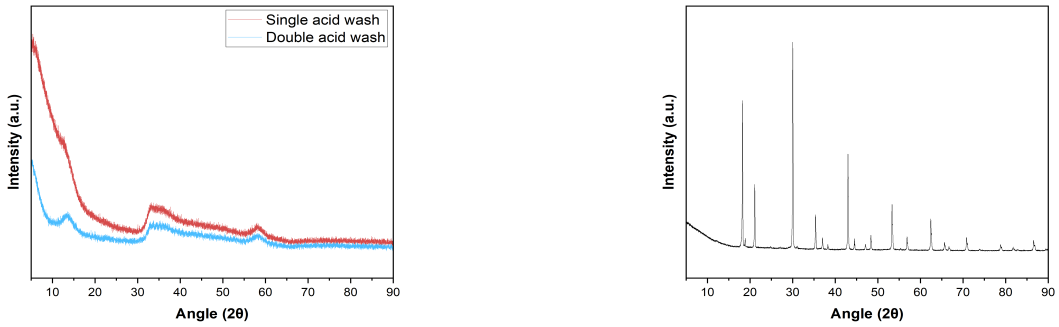

Figure 4.1: XRD pattern of (a) MoS_2 nanomaterial **2**, single acid wash and double acid wash with 2 M HCl and (b) the $K_2NaMoO_3F_3$ core.

the samples came out of the oven and had cooled down to room temperature naturally, the tubes were weighed and compared to the starting weight. The 1 M and 5 M concentrations of H_2SO_4 still had about 1.5 mL of water left after the drying process. However, since a significant amount of core was still visually present in the H_2SO_4 samples, it was decided no to investigate these samples further. Fig 4.2 shows the varying levels of effectiveness in dissolving the core. From this graph, it can be concluded that HNO_3 is most effective in dissolving the core. This data comes from the weight changes of the tubes, weighed empty and weighed after drying. Visually, it was also clear that the HNO_3 samples were most effective in dissolving the core; in the other samples, there was still clearly core material left, while the HNO_3 tubes seemed to be quite empty.

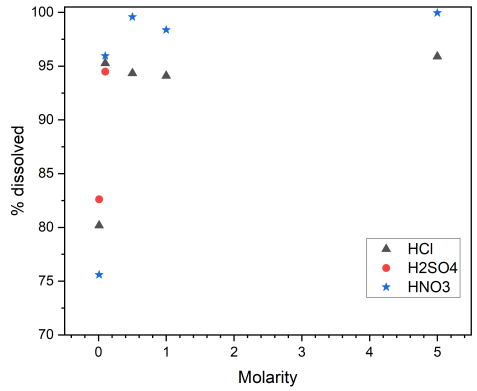

Figure 4.2: Percentage of dissolved $K_2NaMoO_3F_3$ core plotted against the molarity of the respective acid.

From the graph it can be concluded that the 5 M, 1 M and the 0.5 M concentrations of HNO_3 were highly effective in dissolving the core. Since the 5 M concentration did not seem to give significant increase in the dissolving effectiveness compared to the lower concentrations, it was decided to continue with the 1 M and 0.5 M concentrations. This was done considering that a higher concentration of acid also has a higher chance impacting the MoS_2 end product by changing e.g. the morphology or crystallinity. To determine which concentration of HNO_3 would be most suitable to use in the acid wash, 0.5 M or 1 M, the degradation of MoS_2 in each respective acid was tested, as described in 3.2.2. These results can be seen in Table 4.1. The apparent weight increase of 0.54% of the MoS_2 in the 0.5 M solution suggests that some residual water was still present in the product, indicating that the product was not fully dried yet. However, considering the final MoS_2 weight of the 1 M solution is significantly lower than the initial weight, it can be concluded that 0.5 M HNO_3 is the most suitable concentration and acid combination for the acid wash of the core without impacting the MoS_2 material. It was considerded that

the observed weight increase in the 0.5 M sample could be because of nitric salts being left behind after evaporation of the liquid. However, since HNO_3 is a volatile acid [40], it is assumed none to negligible amounts of nitric acids stayed behind and contributed to the weight in the sample.

Table 4.1: Dissolving of MoS_2 in different concentrations of HNO_3.

Molarity	Initial MoS_2 [mg]	Final MoS_2 [mg]	Weight change
0.5 M	50.28	50.55	+0.54%
1 M	50.25	8.52	-83.04%

The synthesis was repeated following the scheme described in 3.2.2, with the 0.5 M HNO_3 mentioned acid wash. The total yield was 533.4 mg. A part of the product was separated before the acid wash. This sample will be referred to as unwashed product, **2UW**, which was used for comparing the sample after acid wash. The rest of the product was acid washed as described in 3.2.2 0.5 HNO_3 acid wash. This final product will be referred to as the acid washed product, **2AW**.

The products were characterized using SEM and TEM, and **2AW** was further characterized using BET. Through EDX analysis with SEM, the elemental composition of the material was determined, both of **2UW** and **2AW**. Based on the respective atom percentages obtained from the SEM EDX analysis, shown in Fig 4.3a, it can be concluded that a substantial amount of the core got washed out by 0.5 M HNO_3; the final **2AW** product consists for 35.06% of Mo and 39.32% of S (74.38% of the total atom composition is thus Mo and S), with only 0.26% K, 0.05% F and 0.1% Na of the core components remaining.
Additionally, EDX analysis with TEM gave a quantification of 48.62% Mo and 48.14% S composition, adding up to a 96.76 atom% of Mo and S. This TEM EDX analysis can be seen in Appendix B.
The SEM images of **2UW** and **2AW** show a slight difference in morphology. The **2UW** spheres (Fig 4.3b) have a varied morphology; some spheres are very spherical and smooth, while others are irregular and rough, with an average diameter of 1.8 μm. In contrast, the spheres in the **2AW** product (Fig 4.3c) have a more uniform morphology, with a predominance of smooth spheres. There are still spheres with a rough surface in the sample, but they are less common than in the **2UW** sample. The **2AW** spheres have an average diameter of 2.5 μm.

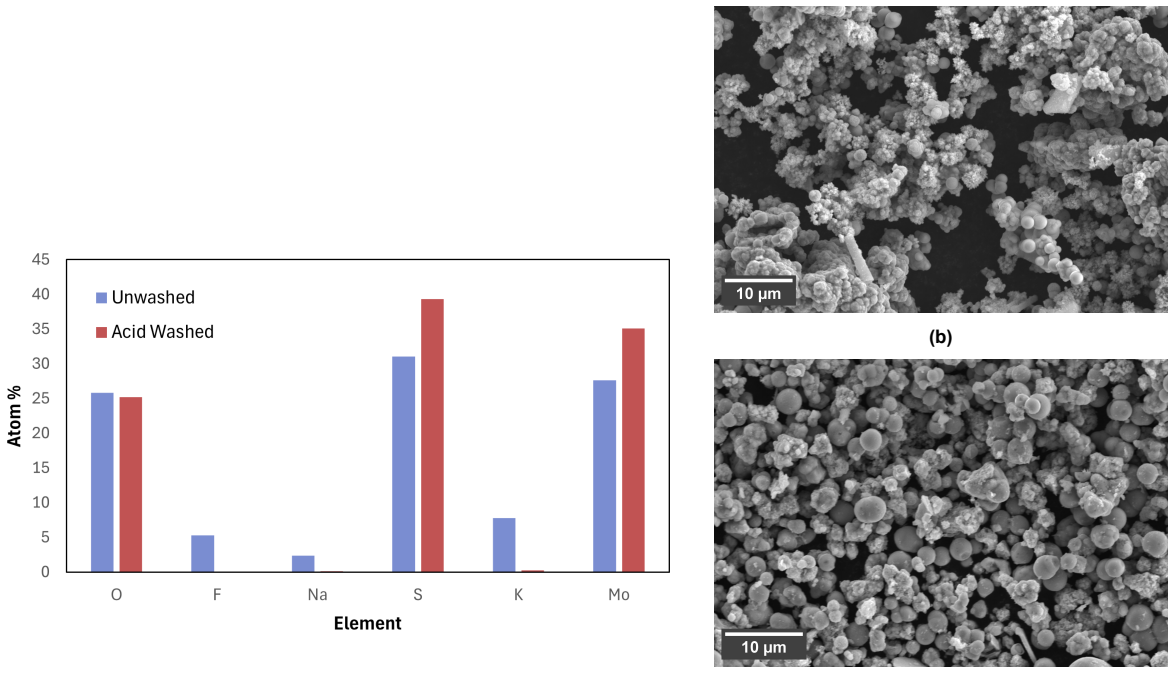

(a) (b) (c)

Figure 4.3: (a) EDX distribution with SEM of elements for **2UW** and **2AW** sample, (b) SEM image of **2UW** sample and (c) SEM image of **2AW** sample.

A TEM grid was made out of **2AW** according to Appendix A and imaged in TEM. The images showed different sizes of particles, ranging from 200 nm to 2700 nm. To determine whether aggregation of particles was the cause behind the large, seemingly solid particles, the TEM sample was subjected to probe sonication for 2 min followed by TEM analysis. The probe sonication, however, did not prove to give the desired hollow results (Fig 4.4). The sample still included solid spheres, as is depicted in Fig 4.4d. Some hollow-like structures were seen, as shown in Fig 4.4c, but the results were not satisfactory in regard to synthesizing hollow spheres.
The BET specific surface area was 74 m^2/g, which differed from the literature [24], where 138 m^2/g was reported.

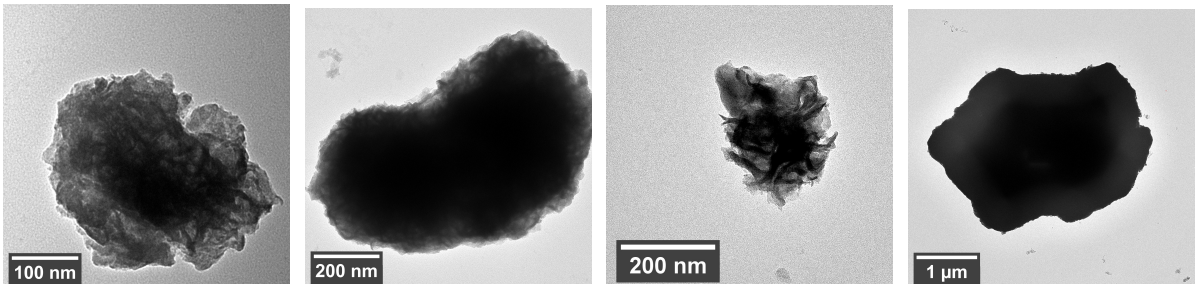

(a) 2AW **(b) 2AW** **(c) 2AW**, probe sonicated **(d) 2AW**, probe sonicated

Figure 4.4: TEM images of (a,b) **2AW** and (c,d) **2AW, probe sonicated**.

The mechanism that the synthesis in the literature [24] is based upon is called the self-sacrificing template method, shown in Fig 4.5. This is a well-known method for synthesizing hollow nanomaterials [41]. However, evidently this mechanism did not work as described. Some characteristics of the product described in the literature [24] did correspond to the product in this synthesis; the surface of the particles is wrinkled, and they show a relatively broad size distribution with a diameter of 0.2-3.4μm . Nevertheless, the spheres synthesized in this report do not appear to be predominantly hollow. Furthermore, the spheres in the literature [24] have a diameter range of 300-800 nm, which is significantly smaller than the spheres synthesized in this report. Also noteworthy is that the **2UW** spheres have a smaller average diameter than the **2AW** spheres, which was not expected. This indicates that the self-sacrifing template method did not work as expected. This reasons for this are uncertain. It is possible that the materials used in the synthesis don't react according to this process, meaning that the MoS_2 does not form a shell around the core, but instead integrates with the core in a disorded and aggregated manner. Dissolving the core substance then does not result in a hollow sphere, but rather leaves behind a disordered structure, that started forming new bonds. This could then explain the bigger diameter of the **2AW** spheres: as the core substance got washed away, the MoS_2 left behind did not have a formed structure anymore since the core was integrated with the MoS_2. The MoS_2 then aggregated and formed larger structures.
Another possible explanation is that the synthesis did in fact work as anticipated, but the acid wash destroyed the formed structures, causing the material to subsequently reform itself into different, larger structures. The initial **2AW** product and the probe sonicated **2AW** product had roughly the same morphology, indicating that any further destruction of morphology by probe sonication did not happen.

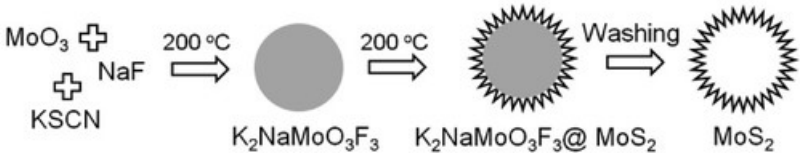

Figure 4.5: Formation process of hollow MoS_2 nanoparticles [24].

4.1.3. Synthesis and Characterization of product 3

Synthesis of the material was done as described in 3.2.3. While adding HCl to the reaction mixture, white solids started forming on the surface of the solution, which became turbid.
The solution was filtered using a Büchner funnel. Two sizes and colours of particles could be observed: small black precipitates (**3S**), as expected when synthesizing MoS_2, and additional larger particles (**3L**), coloured blue and yellow. Separation of the two sized of particles was done manually from the filter paper of the Büchner funnel. The yield for **3S** was 226 mg, and the yield for **3L** was 260 mg. The XRD pattern of **3S** is shown in Appendix B. SEM was done on both **3S** and **3L**. With EDX analysis on the SEM, the elemental composition of **3S** and **3L** was measured. Both can be seen in Appendix B. From the XRD pattern and the EDX analysis of **3S**, it can be concluded that **3S** is indeed MoS_2. EDX analysis of **3L**, while showing a lot of Mo and S, also showed quite a lot of oxygen and even some nitrogen. The nitrogen comes from the degradation of $CS(NH_2)_2$, and the oxygen most likely from some form of molybdenum oxide. From this, it was decided not to go forward with characterization of **3L**, since the EDX indicated that it was not MoS_2.

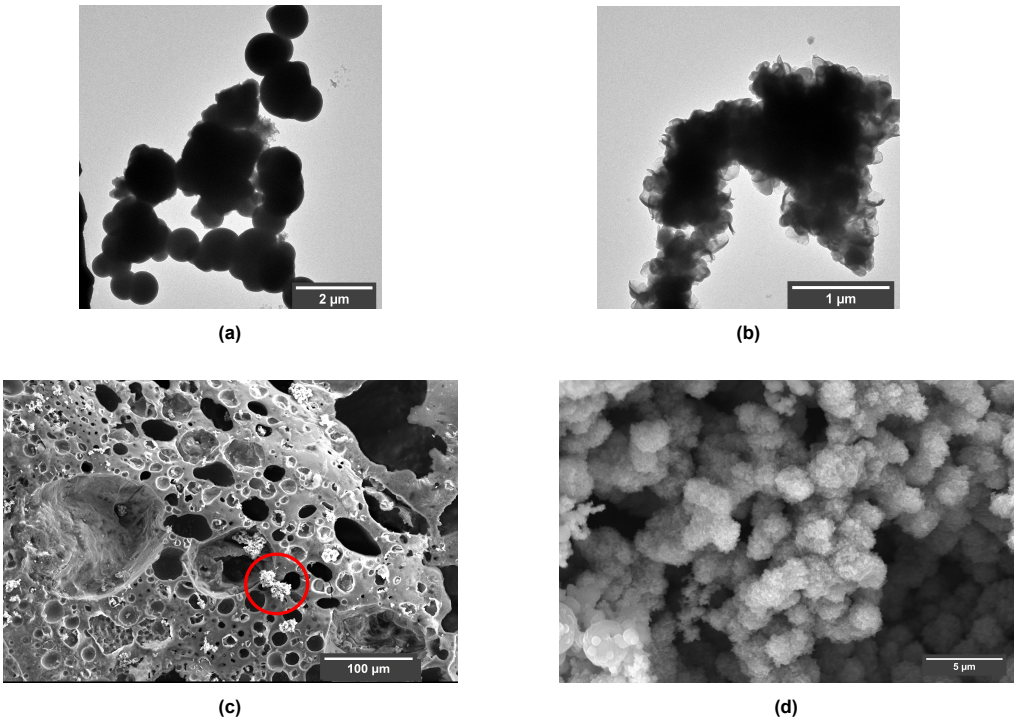

Figure 4.6: Characterization for **3**: (a,b) TEM images of **3S**, (c) SEM image of **3L**, (d) SEM image of **3S**.

The SEM images of **3S** showed the product to be relatively uniform microspheres with diameters ranging between 1 - 2.5 μm (Fig 4.6d). Moreover, a sheet-like structure was observed in parts of the product on TEM images, as seen in Fig 4.6b. However, no hollow structures were seen in the TEM images. The SEM images of **3L** gave a much larger structure. Some MoS_2 microspheres could be found within the larger structure, as is indicated by the red circle in Fig 4.6c. A few questions arise from the results from this experiment, especially around the formation of the **3L** particles.

The **3L** product may have formed because of an unknown reaction with the IL in the oven. The melting temperature of the IL [BMIM]Cl is around 70 °C [42]. After reaction mixture cooled down to room temperature, the IL could have solidified and reacted with the products.
By performing EDX analysis on the SEM, it was observed that **3L** contained a substantial amount of oxygen. This could explain the blue colouring in the product, likely resulting from the oxidation of molybdate [43]. Additionally, according to literature the oxidation process of Mo takes the material through several colour changes, defined as chromism [43]. The oxide's colour appearance changes throughout the process of oxidation and reduction, varying from transparent to yellow and finally gray/blue. So both the blue coloring as well as the yellow coloring could result from molybdenum oxides.

[BMIM]Cl separates in water in a $[BMIM]^+$ cation and a Cl^- anion [37]. The $[BMIM]^+$ cation could also be a source for the yellow colouring in **3L**. The reaction mechanism is described as follows: In the reaction mixture, Cl^- reacts with Na^+, from the molybdenum source Na_2MoO_4, to form NaCl. The $[BMIM]^+$ cations form vesicles in water, acting as a template where MoO_4^{2-} ions can bind to by electrostatic interactions. These binding sites become nucleation domains for the hydrothermal reaction between MoO_4^{2-} and H_2S, which is formed from the decomposition of CH_4N_2S, forming MoS_2 on the surface of the vesicles [37]. With washing of the product, the $[BMIM]^+$ cations should be washed away. However, it seems that $[BMIM]^+$ and MoO_4^{2-} formed $[BMIM]_2MoO_4$, which is observed to be a molybdate-based ionic liquid [44]. This can potentially contribute to the yellow and blue solids seen in the product.
The literature [37] states that the ionic liquid was recovered and reused for subsequent reactions. However, the process of recovery was not specified. The filtered reaction mixture was saved in the fume hood for three weeks to observe if some precipitation or formation of solids would occur, which could later be recovered. But no physical change in the liquid was observed. No separation method was tried.

The sheet-like structures seen on the surface of **3S**, as seen clearly in Fig 4.6b, could contribute to a high surface area. However, since no hollow material was formed, no further investigation to the surface area was carried out.

4.1.4. Synthesis and Characterization of product 4

Synthesis of the material was done as described in 3.2.4. The procedure was repeated thrice to have enough molybdenum-based solid spheres for the next step. The first two rounds of synthesis had a combined yield of 36 mg. This was not enough to continue to the second part of the synthesis, for which 60 mg was needed. The third round, of 16 h stirring, gave a yield of 64 mg of molybdenum-based solid spheres. The extended stirring period seemed to aid dissolving of $C_{10}H_{14}MoO_6$, since the solution looked more homogeneous after the 16 h of stirring. After drying in the oven, some material of the solid spheres was taken before progressing to the second part of the synthesis. When the final solution, **4**, was taken out of the oven, it had a very strong and penetrating smell. TEM samples were made of the molybdenum-based solid spheres and **4** according to Appendix A.

The XRD pattern, shown in Fig 4.7, shows some peaks corresponding to MoS_2, but also some peaks that are not characteristic for MoS_2 materials. This could be due to the impurity of the $C_{10}H_{14}MoO_6$ used, which will be explained in more detail later.
A few unidentified peaks in the XRD pattern could be due to molybdenum oxides forming because of an incomplete conversion of the precursor $C_{10}H_{14}MoO_6$, perhaps due to impurity, or side reactions during the synthesis.

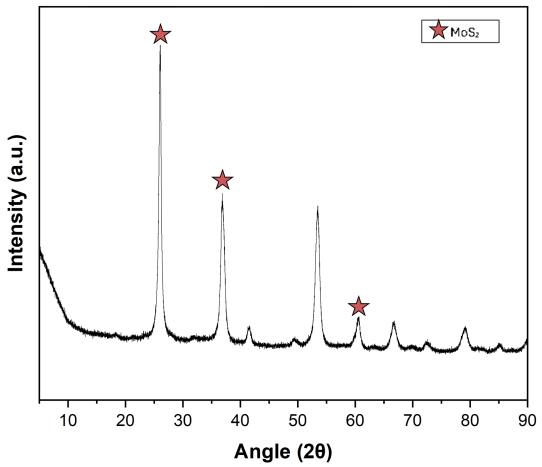

Figure 4.7: XRD pattern of **4**.

XRD patterns of molybdenum oxides found in literature [45],[46] can be found in Appendix B. The peaks around $2\theta = 41, 53,$ and 66 in the XRD pattern of **4** could correspond to MoO_2 in the sample, comparing to the XRD pattern in [46].
TEM images of the MoS_2 nanospheres showed in Fig 4.8b & 4.8c revealed they lost some of the distinct spherical morphology compared to the solid Mo-based spheres. Additionally, some of the MoS_2 spheres aggregated to form larger structures with a total diameter of about 500 nm (Fig 4.8b), while other images showed individual spheres with diameter of about 230 nm. Nanosheets on the surface of the MoS_2 spheres were visible. TEM images of the solid spheres depicted in Fig 4.8a, showed spherical structures with a diameter ranging from $\sim$20-860 nm. Even though some spheres were aggregated, the individual spheres could be distinguished quite well. The resolution of the images was not high enough to determine with certainty whether or not the spheres were smooth, but some spheres appeared to have a rougher surface compared to those described the literature [25].

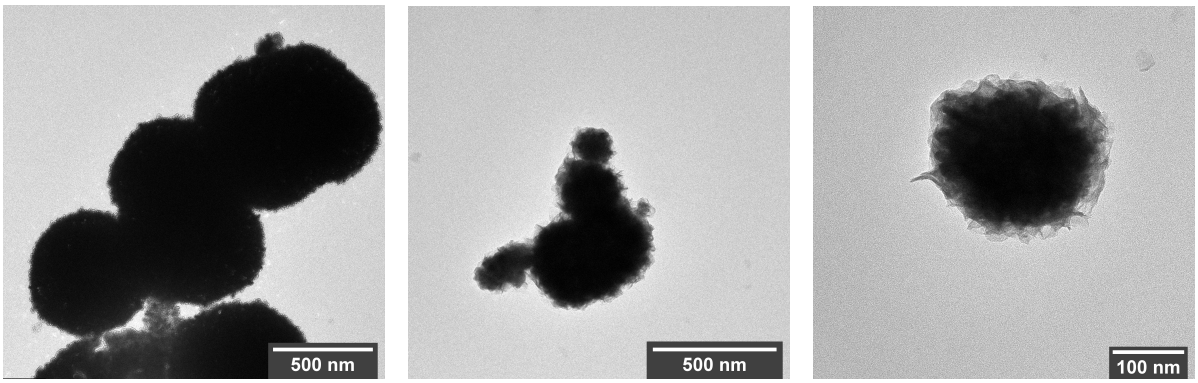

Figure 4.8: TEM images of (a) solid molybdenum-based spheres and (b,c) MoS_2 spheres.

The results observed do not entirely align with the results presented in the literature [25]. Firstly, the fact that three rounds of the first part of the synthesis, making the molybdenum-based solid spheres, were needed to synthesize enough of the solid spheres to continue was unusual. Both the 5 min and 15 min sonication of solution **A** did not result in enough product. Another round of synthesis had to be done. In this round, solution **A** was put on the magnetic stirrer for 16 h before being transferred to the Teflon and put in the oven to try and dissolve the reactant better. The solution was not completely colourless after 16 h of stirring, but it did appear that the $C_{10}H_{14}MoO_6$ was better dissolved in the mixture. This synthesis round had a yield of 64 mg, which was enough to continue the next part of the synthesis. The literature [25] did not state multiple rounds were required, so it can be assumed that it was not necessary. Moreover, the solid molybdenum-based spheres synthesized in the literature [25] were presented to have an average diameter of about 840 nm. While the TEM images of the solid spheres synthesized in this report showed some outliers with a diameter of 840-860 nm, the average diameter was around 520 nm. Smaller spheres with a diameter around 35 nm were also seen. In addition, the MoS_2 hollow spheres presented in the literature [25] had an average diameter of about 940 nm, while the MoS_2 spheres in this report had an average diameter of about 215 nm, with the maximum measured diameter reaching 560 nm. This difference is quite noteworthy, certainly considering the reaction process on which the literature [25] is based is the self-template process, the template here being the molybdenum-based solid spheres.
During the self-templating process, S^{2-} ions react with metal ions, Mo^{4+}, in the solid spheres. The outward diffusion of the Mo^{4+} ions and the inward diffusion of the S^{2-} ions facilitates the reaction forming MoS_2 on the outer region. The continuous outward diffusion of Mo^{4+} ions and inward diffusion of the S^{2-} ions eventually leads to direct transformation of the solid spheres to hollow structures without further active template removal [25]. The process suggests that the end product, created by growing layers on the template, should be bigger than the template itself. The results in the literature [25] demonstrates this; the average diameter of the MoS_2 spheres (940 nm) is bigger than the average diameter of the molybdenum-based solid spheres of the template (840 nm). However, the results in this report show a smaller average diameter in the MoS_2 spheres (215 nm) than the average diameter of the molybdenum-

based solid spheres of the template (520 nm). This suggests that either the synthesis did not follow the predicted self-templating process, or the spheres fell apart somewhere in the process. However, note that this observation of diameters was made based on only a few particles, so it should be taken with some uncertainty.

One possible explanation for these deviating results is the $C_{10}H_{14}MoO_6$ used for synthesis. The substance seemed to be somewhat contaminated with an orange powder, which could be due to the degradation of $C_{10}H_{14}MoO_6$ in presence of air over a long period of time. This could taint the yield of the first part of the synthesis. It could also be a reason for the smaller diameters measured in both the solid spheres and the final MoS_2 spheres: if the reactants are not pure, there is less available to react in the intended reaction. Thus, the solid spheres formed are smaller. Additionally, if the formed spheres are contaminated with unintended substances, that might intervene with the ion diffusion and thus with the self-templating process. With this explanation, it can be presumed that the synthesis carried out in this report did not follow the predicted self-templating process completely.
XRD analysis was done on the used $C_{10}H_{14}MoO_6$ to check the pattern. The pattern can be found in Appendix B. It was difficult to compare the XRD pattern to literature, as no clear XRD pattern was found for pure $C_{10}H_{14}MoO_6$. However, is is plausible that $C_{10}H_{14}MoO_6$ oxidized to form MoO_3, which could explain the visual orange contamination in the $C_{10}H_{14}MoO_6$ powder, since MoO_3 is reported in literature to have an orange colour [47],[48]. Some peaks in the XRD pattern of the $C_{10}H_{14}MoO_6$ used in this report overlap with the peaks for MoO_3 XRD patterns found in literature [45]. This could be a contamination in the $C_{10}H_{14}MoO_6$ powder. However, XRD characterization of new and pure $C_{10}H_{14}MoO_6$ powder should be done before any such assumptions can be proven.

4.1.5. Synthesis and Characterization of product 5

Synthesis of the material was done as described in 3.2.5.

Synthesis and Characterization of product 5a

Two rounds of synthesis of the $MnCO_3$ solid spheres were done. In the first round of synthesis, the normal values of the reactants were used as mentioned in the literature [26]. This round had a yield of 1845 mg. Products with a stirring time of t = 15 min and t = 30 min were imaged. The XRD of the t = 30 product, which can be found in Appendix B, showed that the product was indeed $MnCO_3$, and TEM showed that the morphology of the product was indeed spherical. However, the TEM also showed that the t = 30 min product was very aggregated, while the t = 15 min product appeared to be less so. These TEM images can be found in Appendix B.
The second round of synthesis was done with half of all the values of the reactants mentioned in the literature [26] and with 15 min of stirring. The yield for this synthesis was 1253 mg. SEM EDX analysis showed that the elemental composition comprised of Mn, C and O, as expected, but there was also some Cl and Na left from the reactants. This can be attributed to insufficient washing, but is not expected to cause trouble for the rest of the synthesis. The EDX analysis can be found in Appendix B.

TEM images, seen in Fig 4.9a confirmed that the $MnCO_3$ spheres were less aggregated now, showing spheres with an average diameter of 460 nm.
With these t = 15 min $MnCO_3$ spheres, the second part of the synthesis was done. When the solution came out of the oven, 1 mL of solution was taken out, centrifugally washed with milliQ and separated (unwashed sample, **UW5a**) while the rest of the solution was washed with 1.0 M HCl, resulting in product **5a**. The total yield of this synthesis was 274.6 mg. XRD was done on **5a** and compared to the literature [26], proving that the product was indeed MoS_2. The XRD pattern can be found in Appendix B. 100 mg of **5a** was taken out for BET analysis. The morphology of **UW5a** and **5a** was further characterized by TEM. TEM images of **UW5a** (MoS_2@$MnCO_3$ spheres) are shown in Fig 4.9b. Fig 4.9c shows a TEM image of the product **5a**.

As seen in Fig 4.9c, the product **5a** seemed to be partially hollow on TEM images. The product did not really have the distinct spherical morphology anymore, but appeared to consist of MoS_2 sheets stacked together. There could be two reasons for this: during the acid wash, the spheres fell apart, losing their morpology, and the separate MoS_2 sheets aggregated to form the strucures seen in the images. The other possible reason is that the spheres collapsed in the vacuum of the TEM. To test this, the spheres were imaged with less beam intensity. When using lower beam intensity, the electron dose rate on the sample is lowered, reducing the damage depth that the focused beam can induce on the sample [49].

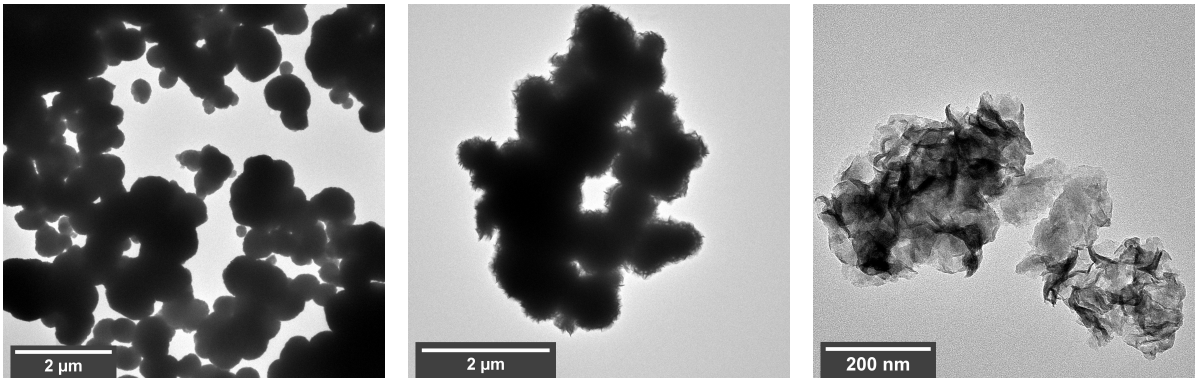

Figure 4.9: TEM images of (a) $MnCO_3$ solid spheres, (b) MoS_2@MnS spheres and (c) MoS_2 spheres.

This imaging did show different morphology, as seen in Fig 4.10. The samples appeared to have more structural integrity under low-intensity conditions, indicating that the high beam intensity conditions in the TEM caused some damage to the sample. The product does have hollow parts, but also parts that seem to be quite solid.

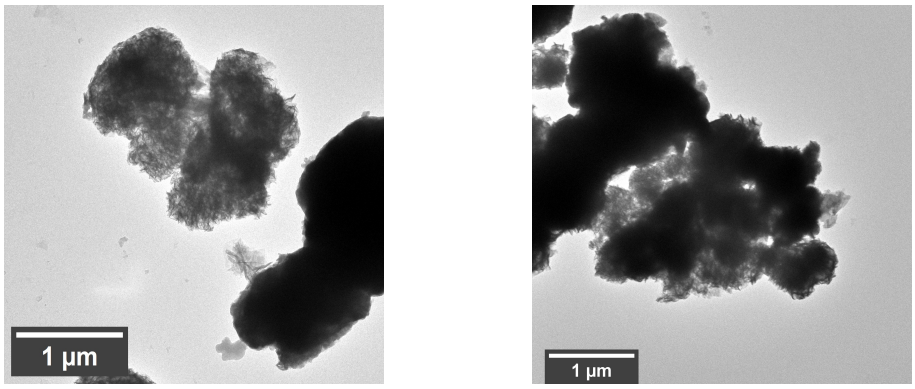

Figure 4.10: (a) size distribution of the different cubes, (b) TEM image of the t = 15 $MnCO_3$ cubes.

The literature [26] did not mention any specific stirring time for the first part of the synthesis, only to stop stirring as soon as the reaction was finished. However, according to another article describing the same reaction, the reaction would take a maximum of 3 h [50]. White solids started forming almost instantly after addition of the $MnCl_2$ solution to the Na_2CO_3 solution. The stirring in this report was stopped at t = 15 min and t = 30 min. Since this gave the needed product to continue with synthesis and characterization, this was deemed adequate stirring time for this report. The stirring time could be adapted to the type of spheres that is needed for a further synthesis; if bigger spheres are needed for a certain purpose, longer stirring time can be allowed, and vice versa for smaller spheres.

Synthesis and Characterization of product 5b

Once the reaction mixture was put in the heated water bath, a turbid solution started forming almost instantly. The XRD pattern of the t = 16 h heated product, which can be found in Appendix B, was analysed and compared to the literature [27] and it was observed that the product was indeed $MnCO_3$. The SEM and TEM images showed very distinct cubical morphology. SEM EDX analysis additionally confirmed that the elemental composition of the synthesized cubes was $MnCO_3$, and can be found in Appendix B. A TEM image of the t = 16 h solid $MnCO_3$ cubes can be seen in B. The cubes were measured with ImageJ to have an average edge length of 9 μm. This is quite big, and the expectation was that the cubes would be smaller if they were heated for a shorter time. For the t = 2 h synthesis, the yield was 265 mg. TEM images of the cubes were again measured with ImageJ and the average edge length was now 4.4 μm. A TEM image of the t = 3 h cubes can be seen in Fig 4.11b. In addition

to the smaller edge length, the variability of the measured values was lower, as can be seen in Fig 4.11a. Since it is easier to predict the behaviour of a homogeneous material, lower variability in size is desirable.

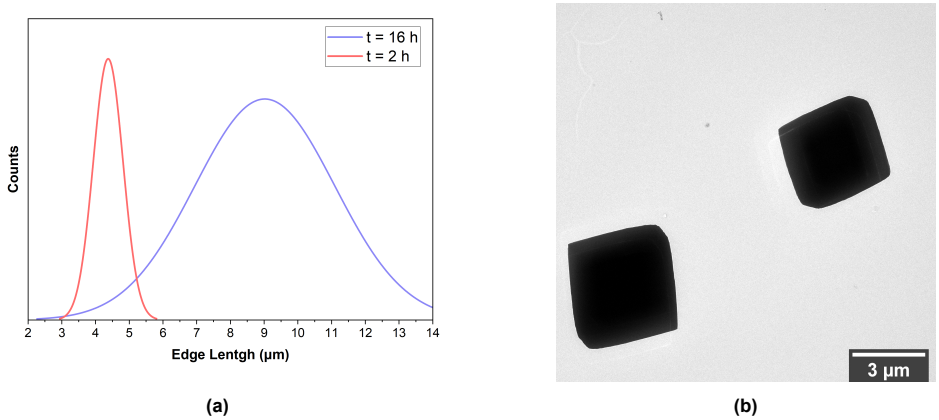

Figure 4.11: (a) size distribution of the different cubes, (b) TEM image of the t = 2 h $MnCO_3$ cubes.

Now that it was confirmed with XRD and TEM that the cubes were indeed $MnCO_3$ and had smaller edge length, the next steps of the synthesis were carried out to grow a MoS_2 shell on the microcubes. As was done in the synthesis of the spheres, a small amount of product was separated and washed before the acid wash (unwashed sample, **UW5b**). The rest of the product was washed with 1.0 M HCl as mentioned in 3.2.5, resulting in product **5b**. The total yield for this synthesis was 467.16 mg. The XRD pattern of the acid washed sample, which can be found in Appendix B, proved that the product was indeed MoS_2.

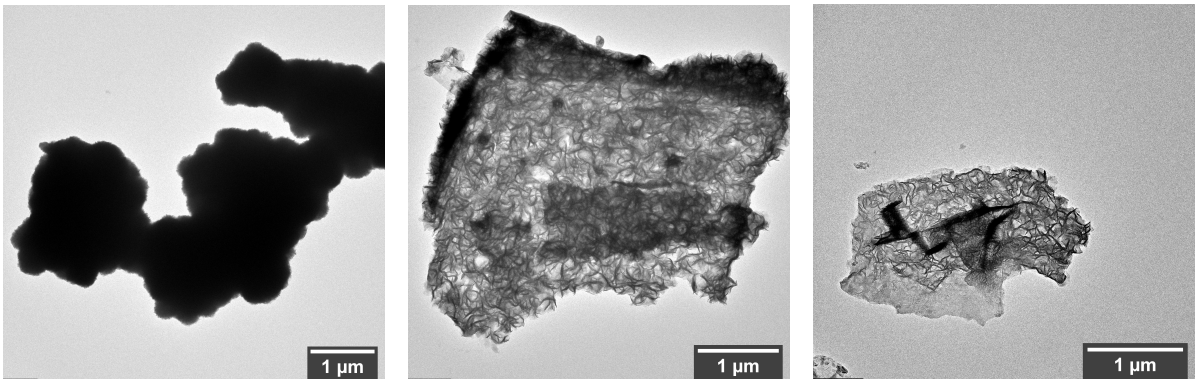

Figure 4.12: TEM images of (a) MoS_2@MnS cubes and (b,c) MoS_2 cubes.

TEM images of both **UW5b** and **5b** showed that the cubes had lost their cubical morphology, as seen in Fig 4.12. **5b** did appear to have some hollow structures with sheets of MoS_2 on the surface. In some material in **5b**, the cubical morphology was still somewhat distinguishable, as seen in Fig 4.12b, while in other parts of the product the cubical morphology had been lost almost entirely, as seen in Fig 4.12c. With a bit of imagination, the cubical form can still be spotted in this, however it can be said that the cubical form was largely lost. The structures that were imaged did seem to be partly hollow. However, given the substantial degree of structural loss it was decided to continue with other samples for further testing.

In the literature [27], the obtained MoS_2 microcubes were further annealed in a tube furnace (800 °C, 5% H_2 atmosphere balanced by N_2). Since there was no tube furnace available for this synthesis, this step was skipped. Annealing could help with mechanical stability and with crystallinity of the product, potentially helping the cubes retain their morphology. When comparing the XRD pattern of the liter-

ature's MoS_2[27] with the one from this report, the literature [27] does not show a significantly more crystalline pattern than the pattern of this report. So the cubes seem to have an equal measure of crystallinity. Nevertheless, it is clear that the structure of the MoS_2 end product in this report does not correspond to the cubical structure depicted in the literature [27]. The reason for this could be the additional annealing step. However, the structure could also be broken by the sonication during the acid washings. In the literature [27], the acid washings were done by stirring instead of sonication, so it cannot be said with certainty that the cubes could withstand sonication in acid. Thus this could also be a possible reason for the structural loss.
However, even before the acid wash the cubes lost some of their morphology, as seen in Fig 4.12a. This is also before the annealing step in the literature[27]. This structural loss could also be caused by the high vacuum in TEM, that made the cubes collapse.

Both the reaction mixtures for the cubes and the spheres had a very strong malodorous smell upon being taken out of the oven. This smell is likely coming from H_2S or SO_2, sulfur containing compounds that can be produced due to the decomposition of the thiol group of L-cysteine (-SH functional group). This is released as a gas. This gas had most likely leaked out of the Teflon chamber, hereby contaminating the inner part of the autoclave and diffusing the smell into the lab. Apart from the unpleasant smell, these gasses are toxic in certain concentrations in the air (according to OSHA guidelines, 20 ppm for H_2S and 5ppm for SO_2 as 8-hour time weighted average[51]). Fortunately, the labs were equipped with adequate ventilation and of the 0.0103 moles of sulfur in the reaction, from the 1.25 gr of L-cysteine, most of it reacted with Mo to form MoS_2 according to the observed yields.

4.2. Stability

Stability of the molybdenum materials was tested for two samples, namely **2** and **5a**. Only these materials were tested, because these two showed the most potential for the hollow MoS_2 nanomaterials striven for in this report. The tests were done as described in 3.3. The results of the stability tests are shown in Fig 4.13.
For the consecutive washes, the percentage of Mo breakthrough was highest in the first wash, subsequently decreasing with successive washes. As can be seen in the Fig 4.13, **2** exhibited more breakthrough than **5a**. Nonetheless, both samples had low breakthrough percentages and showed a downward trend with each consecutive wash.

Moreover, time stability was also tested on sampled **2** and **5a**. As can be seen in Fig 4.13b, in these washes the Mo breakthrough for both samples was very comparable. Up until the 16 h wash cycle, the samples vary in higher and lower breakthrough. One remarkable result is the 24 h wash in sample **2**. It is not necessarily strange for the 24 h wash to have a relatively higher breakthrough. However, the degree in which the percentage differs from the 16 h wash is very high. Looking at the **5a** results, the 24 h wash barely differs from the 16 h wash. The uncertainty for the 24 h wash of 2 is also quite high. The exact reasons for this high percentage are not sure, but one possible explanation could be the saturation effect. Somewhere between 16 h and 24 h, there could be a saturation effect on the material. As a material gets saturated in water, the dynamic stability can decrease [52]. If soaked for longer than the saturation time, the release and thus breakthrough of molybdenum in the material increases significantly. Supposing the saturation time of sample **2** lies somewhere between 16 h and 24 h, the difference between the two wash cycles can be explained. This hypothetical saturation time is quite problematic for the intended application of the nanomaterial, as in a generator setting the material needs to maintain its stability for extraction over extended periods of time. In general, hospitals make their extractions every 24 h [18], and a generator is kept for about two weeks. Thus the material needs to maintain its stability for at least 24 h, the time of each extraction, but in final applications longer, to be utilized in generators for multiple extractions. Therefore, to determine if the sample is suitable for generator applications, further investigation should be done into the saturation time of **2**.

When comparing the Mo breakthrough percentages of the **2** and **5a** samples, it is important to note a few things. The BET surface area of **2** was analysed to be 74 m^2/g, while **5** had a much lower surface area of 18 m^2/g. Considering the higher surface area of **2**, it justifies a higher breakthrough percentage. A higher surface area provides more active sites for the solvent to interact with the material, potentially leading to higher breakthrough percentage during elution. However, a higher surface area not only means higher breakthrough of Mo, but also higher extraction potential of ^{99m}Tc. This is of course a

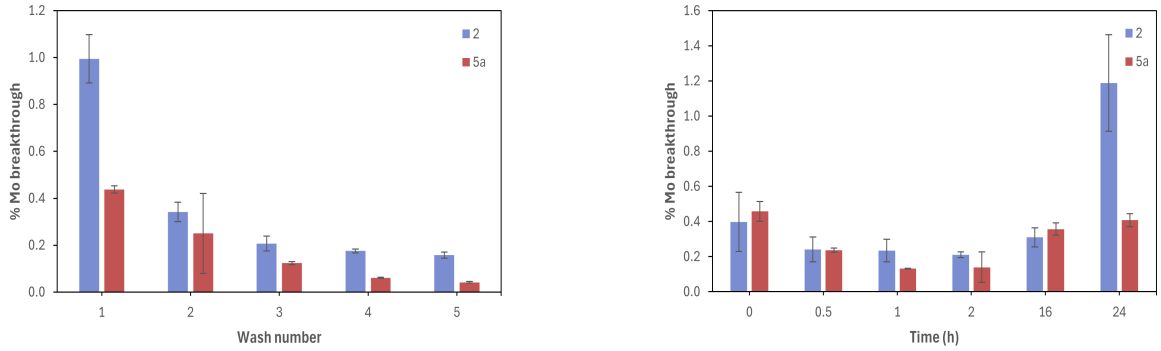

Figure 4.13: Percentage of Mo breakthrough in milliQ (a) wash number and (b) wash cycles with soaking time.

desirable trait for the materials. Also note the interesting comparison that can be made with the Mo breakthrough in solid MoS_2 samples. A solid MoS_2 material previously synthesized by Gauri [53], had a BET specific surface area of 5.8 m^2/g. This sample had Mo breakthrough percentages of 0.056% at the 10th wash and at the 20 h soak. This value is much lower than the breakthrough percentages presented here. This could be explained by the hollowness of the materials tested in this report. If a material is hollow, it has more accessible surface area. Thus, more area from which molybdenum can break through. In a solid sample, the solvent has less accessible area, only the outer layer, resulting in less interaction with the molybdenum. A comparison could be made relative to BET specific surface area, by normalising each Mo breakthrough percentage with its respective surface area for each sample. This is done in Table 4.2. The hollow-like materials seem to perform better under the number washes, but have a worse stability under the wash cycles with soaking time than the solid MoS_2 materials. This could be due to the many more active sites in which the solvent can interact with the material when it is hollow, and the above-mentioned possible saturation time. However, note that the number of consecutive washes and soaking time of **2** and **5a** differ from the solid sample, so a direct comparison cannot be made. The higher breakthrough in the wash cycles with soaking time can be attributed to the hollowness of the materials tested in this report.

Table 4.2: Breakthrough data.

Sample	Surface area (m^2/g)	Breakthrough last wash (%)	Breakthrough longest soak (%)	Normalized breakthrough last wash (%)	Normalized breakthrough longest soak (%)
2	74	0.157 (5th)	1.189 (24 h)	0.002 (5th)	0.016 (24 h)
5a	18	0.042 (5th)	0.408 (24 h)	0.002 (5th)	0.023 (24 h)
Solid	5.8	0.056 (10th)	0.056 (20 h)	0.010 (10th)	0.010 (20 h)

Furthermore, SEM images of **2** confirmed that no notable morphological changes were observed in the sample after the washings. The SEM images can be seen in Appendix B.

The acceptable limit of ^{99}Mo breakthrough in a ^{99}Mo/^{99m}Tc generator varies throughout the years in literature and regulatory bodies. A maximal limit of 1.0μCi ^{99}Mo/mCi ^{99m}Tc, not to exceed 5μCi per human dose at the time of injection was found in literature from 2012 [54], but more recent value is a limit of less than 0.15 μCi ^{99}Mo/ mCi ^{99m}Tc at the administration time, following USP's guidelines (United Stated Pharmacopeia) from 2020 [55]. This translates to a maximal contamination percentage of 0.1% and 0.015% in the ^{99m}Tc eluate. A generator based on $(n,\gamma)^{99}$Mo is already stated to have a bigger problem with ^{99}Mo breakthrough than the fission-based generators [54]. This is mainly attributed to the low specific activity of the ^{99}Mo used. A lower specific activity means there is less radioactive decay occurring per unit time in comparison to high specific activity ^{99}Mo. So even if the absolute ^{99}Mo

breakthrough is the same, the relative ^{99}Mo breakthrough to the amount of ^{99m}Tc present in the eluent may be higher. The breakthrough percentages presented in Fig 4.13 are not for ^{99}Mo but for natural molybdenum breakthrough. The samples tested for stability were not irradiated. So, while these results provide an understanding of the material's overall stability, further investigation is necessary to assess the breakthrough behaviour of ^{99}Mo and determine whether the breakthrough percentages are low enough for medical use.

4.3. ^{99}Mo and ^{99m}Tc extraction

30 mg of both **2** and **5a** was irradiated for 10 h, with a cooling time of 12 h.
The samples were treated as described in 3.4. The ROI's on the Ge-detector were selected according to the energies of emitted γ's [56]: for ^{99}Mo the ROI was set to 726.4 - 758.5 keV and for ^{99m}Tc the ROI was set to 135.6 - 145.7 keV. The extraction yield percentages of ^{99}Mo are shown in Fig 4.14 below. The yields are calculated from the number of counts of ^{99}Mo in the entire sample and the number of counts of ^{99}Mo in the extraction liquid.

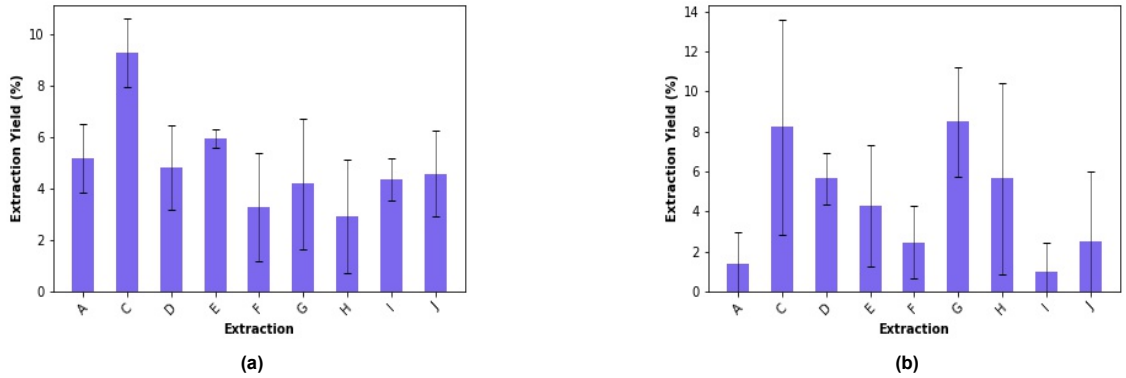

Figure 4.14: Percentage of Mo extraction yield in the measured washings of (a) sample **2** and (b) sample **5a**.

Because the centrifugal separation did not work well, the switch was made to PES centrifugal filter for separation after the first wash. Five days after irradiation, the first extraction was done, extraction A. The milliQ had some trouble filtering through the PES filter. Because of this, the second extraction, B, could not be measured because of time constraints. Thus, extraction B was done but not measured on the Ge-detector.
From extraction C onwards, filtering went smoother due to the fresh milliQ put on top of the material after each extraction. Of the two extractions made each day, the first was the most important to get extraction data, the second extraction was to flush out any remaining ^{99}Mo and ^{99m}Tc, to make the extraction complete. This also shows in the extraction yields: usually, the second extraction of the day (D,F,H,J) has lower extraction yield than the first (A,C,E,G,I) since most loose material already got flushed out at the first extraction. Notably, for extractions I and J, the second extraction is slightly higher for **2** and clearly higher for **5a**. This can be explained by the decreased activity of the samples at the time these extractions were made, which was 10 days after irradiation. With a lower activity, the measurement uncertainty of the Ge-detector increases. The average uncertainties for sample **2** were 14% for extraction I and 12% for extraction J. The average uncertainties for sample **5a** were 17% for extraction I and 21% for extraction J. The highest uncertainties were seen for the ^{99}Mo peak in the liquid extractions, where they could reach an uncertainty of 45%. The counts for ^{99}Mo $\gamma's$ were very low at these measurements. The uncertainty of the number of counts detected is proportional to the inverse square root of the number of counts, as follows from Poisson statistics [57]. For these low counts measurements, the uncertainty becomes very high and can thus help explain the deviating results in these last two measurements.
What also should be noticed is the high standard deviations in most of the measurements. This can be attributed to several factors. One major contributer is, again, the uncertainties of the measurements, which range from 1.3% to 45%. These uncertainties arise from various sources, such as low counts rates, detector efficiency and small geometry differences. The dead time τ should also be considered

as reason for the large deviations between measurements. During the dead time, the detector is unable to detect new counts due to processing time of pulses. However, the highest dead time for extraction A-J measurements was 0.92%. Compared to the uncertainty values, the impact of the dead time can be considered negligible. Additionally, the statistical variations of radioactive decay can also be a source for the high standard deviations, particularly for low count rates.

Another possible reason for the large standard deviation can be small differences in geometry per measurement. The Ge-detector is very sensitive to this. Additionally, the curious observation was made that the sum of the **S** and **L** counts was almost always, with very few exceptions, higher than the **AC** measurement. This could also possibly be attributed to the geometry. To try and determine whether the observed difference in counts between **AC** and **S** + **L** could be attributed to the small geometry differences, an extra measurements was taken for two extractions, J and K, measurement IV in Fig 3.3. In this measurement, the PES filter tube was lifted from the eppendorf, and the extraction liquid was pipetted back in the eppendorf after which the PES filter was placed back on top.

After measuring and decay correcting the results of measurement IV, the number of counts was, for all except two of the 12 measurement, in between the counts for **AC** and the sum of **L** counts and **S** counts. Taking into account the wide range of uncertainties associated with the measurements, it is likely that the observed variations in measurements arise mostly from these uncertainties. While small geometry differences can contribute to these variations, the fact that measurement IV fell within the range of **AC** counts and **S+L** counts for most cases suggests that the geometry differences played a less significant role in the observed results.

Regrettably, not enough measurements were taken in this report to be able to calculate extraction yields for ^{99m}Tc. ^{99}Mo and ^{99m}Tc reach a transient radioactive equilibrium after about six half-lives of ^{99m}Tc, which is after about 36 hours. To be able to reconstruct the graph of the decay and production of ^{99m}Tc and back calculate the activity and extraction yield, measurements at t = 0 and at equilibrium, t > 36 h, need to be taken. For extractions I and G, such measurements were taken. However, the activity of the samples at equilibrium was very low resulting in very high uncertainties of the measurements at equilibrium. With a minimal uncertainty of 30% and a maximal uncertainty of 222%, the data was not reliable enough to make any accurate calculations. Therefore, results regarding the extraction yield for ^{99m}Tc cannot be given, nor can a ratio of ^{99}Mo/^{99m}Tc in the eluent be calculated. However, it is notable that the counts for ^{99m}Tc γ emissions were relatively higher than those for ^{99}Mo γ's in the extraction liquid. While absolute calculations are not possible with this data, it does suggest promising prospects for further research, hinting at high radionuclide production and extraction potential. However, the contamination percentage of the ^{99m}Tc eluent may be alarmingly high. The $(n,\gamma)^{99}$Mo based generators are, as mentioned above, hypothesized to have bigger problems with contamination percentages [54], so other solutions to this problem may be necessary, finding a way to work with this higher contamination percentage.

5

Conclusion and Recommendations

Conclusion

The use of ^{99m}Tc in current nuclear medicine procedures is undeniably crucial. The current fission-based production route faces several challenges, such as supply chain reliability issues, proliferation risk and significant radioactive waste generation. To ensure the reliable availability of ^{99m}Tc, new production routes should be explored. One promising production route is the use of enriched ^{98}Mo- or ^{100}Mo-based nanomaterials as the source for ^{99m}Tc.

Within this report, five synthesis methods have been tried to synthesize hollow MoS_2 nanomaterials. MoS_2 has been successfully synthesized and characterized in four schemes. **2**,**3**,**4** and **5a** exhibited a spherical morphology, while **5b** exhibited a cubical morphology. **1** was not successfully separated nor characterized. Hollow nanomaterials were not completely achieved in this report. MoS_2 sheets were seen on the surface of **2**, **3**, **4**, **5a** and **5b**. These nanosheets could help with a higher surface area. Synthesis of nanoporous MoS_2 material is not confirmed, since characterization was not possible for product **1**. Partial hollow materials were seen in **2**, **5a** and **5b**. While this is not yet the final desired results, it is a step towards the hollow structures that are needed for the application in ^{99m}Tc production. The MoS_2 nanomaterials that were tested for stability, namely **2** and **5a**, demonstrated low Mo breakthrough in milliQ. In the cycle washes, the materials showed lower breakthrough than solid MoS_2 sample, but in wash cycles with time soaking the partial hollow materials showed higher breakthrough than the solid sample. Additionally, both samples followed a downward trend through the five washes, hinting that most loose ^{99}Mo will be flushed out in the first few washes, which is advantageous to minimize ^{99}Mo contamination in subsequent eluents with ^{99m}Tc. Nevertheless, the relatively higher breakthrough percentages for the wash cycles with soaking time, particularly the longer soaking times, could pose a problem for the generator applications with multiple extractions over a longer period of time. Samples **2** and **5a** were irradiated. **2** was measured to have between 2.9-9.3% of the total ^{99}Mo in the extraction liquid. **5a** was measured to have between 1-8.5% of the total ^{99}Mo in the extraction liquid. Based on the measured counts for ^{99m}Tc, the materials demonstrate an optimistic potential for high ^{99m}Tc radionuclide extraction efficiency. However, the conceptual problem of high ^{99}Mo contamination percentage needs to be addressed and researched further. Other solutions to this problem may be necessary, finding a way to work with this higher contamination percentage. Nevertheless, before any conclusion about extraction yields and contamination percentages can be confirmed, equilibrium measurements of the extraction liquid need to be taken in order to calculate the ^{99m}Tc extraction yield. Only then a valuable conclusion can be drawn, allowing a ^{99}Mo/^{99m}Tc ratio to be calculated.

The two qualifying conditions for generator usable material are a high surface-to-volume ratio and a high radionuclide extraction potential. The materials synthesized in this report do not fully meet the requirements yet, but they show potential for the future of MoS_2 materials in ^{99}Mo/^{99m}Tc generators. If they prove not to be directly suitable, then to be a source of learning and development, guiding future research to achieve the desired properties in nanomaterials.

Recommendations for further research

Following the findings and work done here, a few recommendations are made for further research.

Nanoporous materials A nanoporous structure can be a good method to gain surface area, with their high surface area-to volume ratio. Additionally, literature states nanoporous material to have strong structural integrity [58]. Thus, it could be an interesting synthesis method to explore further. For method **1**, where synthesis of a nanoporous material was attempted, other filtration methods can be tried. In this thesis, only filtering by Büchner funnel and centrifugation was tried. Ultrafiltration can be tried to filter the nanoparticles. Ultrafiltration is a pressure-driven transport process, used to separate colloids with particles ranging from 2-1000 nm [59], and could therefore potentially separate the particles from the liquid. Additionally, new synthesis methods for nanoporous Mo-based nanomaterials could be explored.

Ionic Liquids The use of ionic liquids could pose an interesting templating tactic. The distinct properties of an ionic liquid are strongly dependent on the species of cations and anions. This opens up a huge variety of unique properties [60]. While in this report the resulting spheres synthesized with an ionic liquid template were not hollow, further work with ionic liquids could be interesting and valuable to explore for hollow molybdenum-based nanomaterials, due to the potentials for customized designs.

Exploring other acid wash methods It is recommended to explore alternative acid wash methods, as there is uncertainty regarding whether the performed acid washing processes may have contributed to the destruction or deformation of the morphology in some of the experiments.

Extra characterization analysis Some more characterization should be done to get answers to certain questions arisen from this report. An XRD pattern of the **UW5a** and **UW5b** samples would help determine if they indeed comprise of MnS@MoS_2, which can in turn say more about the underlying synthesis reactions. Furthermore, XRD and SEM analysis of the irradiated samples **2** and **5a** can determine if the samples underwent any structural or morphological changes induced by irradiation. This information is crucial to establish if these materials are actually suited for irradiation and extraction. Additionally, more analysis should be done on the **5b** microcubes. Although they did loose their cubical morphology, the product did exhibit quite some hollow areas. It is therefore worthwhile to look further into where in the process they lost their morphology, and what kind of impact that will have on the stability and surface area. For example, low-beam intensity TEM imaging can be employed on sample **5b**, to see if the TEM conditions are a reason for the loss of cubical structure. Lastly, the time stability of the materials needs to be closely examined, to evaluate the long-term performance and reliability of the materials.

Self-templating process The self-templating process is a mechanism described in the literature used for method 4 [25]. When using a diffusion reaction to make the material hollow, the problem of having to wash away a core is solved. The reaction sounds ideal in theory, but proves challenging to achieve in synthesis. Another round of synthesis of method 4 (3.2.4) is recommended, with the $C_{10}H_{14}MoO_6$ used in pure form. If the synthesis then still does not give the desired result, nor shows potential to do so with a few modifications of the synthesis, the method should be abandoned. However, other self-templating mechanisms can be explored.

Extraction measurements Additional measurements need to be taken of the irradiated materials. Measurements at t = 0 and at equilibrium will make it possible to calculate extraction yields for ^{99m}Tc and to calculate the ^{99}Mo^{99m}Tc ratio in the extractions. Consequently, conclusions can then be drawn whether or not the materials have a sufficiently high ^{99m}Tc extraction yield and low enough ^{99}Mo breakthrough to be considered suitable materials for a ^{99}Mo/^{99m}Tc generator. Moreover, if any potential materials do not demonstrate improved contamination percentages, it may be necessary to develop methods to work with the higher contamination levels. A suggestion for this could be the Post Elution Concentration techniques, which can enhance the radioactive concentration of $^{99m}TcO^{4-}$ in the eluent from a $(n,\gamma)^{99}$Mo generator, possibly solving the problem of high contamination levels [61].

Finding inspiration in the biological world Throughout evolution, nature has continually solved complex problems through ingenious strategies and structures. In the fields of material science and nanotechnology, the biological world offers a cornucopia of inspiration for innovative solutions. For

instance, consider the lungs, which cover an impressive surface area estimated between 70-140 m^2 within the modest volume of 2-3 L [62]. By using bio-inspiration for hollow Mo-based nanomaterials, researchers could generate innovative and interesting ideas to achieve the goal.

References

[1] Ole K Hjelstuen. “Technetium-99m chelators in nuclear medicine. A review”. In: *Analyst* 120.3 (1995), pp. 863–866.

[2] Alessandra Boschi et al. “Recent achievements in Tc-99m radiopharmaceutical direct production by medical cyclotrons”. In: *Drug development and industrial pharmacy* 43 (2017), pp. 1402–1412. DOI: https://doi.org/10.1080/03639045.2017.1323911.

[3] A. G. Jones. “Technetium in Nuclear Medicine”. In: *Radiochimica Acta* 70-71.s1 (1995), pp. 289–298. DOI: doi:10.1524/ract.1995.7071.s1.289.

[4] ALEXANDER Gottschalk. “Technetium-99m in clinical nuclear medicine”. In: *Annual Review of Medicine* 20.1 (1969), pp. 131–139.

[5] International Atomic Energy Agency - Human Health Campus. *^{99}Mo - ^{99m}Tc radionuclide principles*. May 13. 2024. URL: https://humanhealth.iaea.org/HHW/Radiopharmacy/VirRad/Eluting_the_Generator/Generator_Module/99Mo_-_99mTc_radionuclide_principles/index.html.

[6] Maroor Raghavan Ambikalmajan Pillai, Ashutosh Dash, and FF Russ Knapp. “Sustained availability of ^{99m}Tc: possible paths forward”. In: *Journal of Nuclear Medicine* 54.2 (2013), pp. 313–323.

[7] Seung-Kon Lee, Gerd J. Beyer, and Jun Sig Lee. “Development of Industrial-Scale Fission 99Mo Production Process Using Low Enriched Uranium Target”. In: *Nuclear Engineering and Technology* 48.3 (2016), pp. 613–623. ISSN: 1738-5733. DOI: https://doi.org/10.1016/j.net.2016.04.006.

[8] National Research Council et al. “Medical isotope production without highly enriched uranium”. In: (2009).

[9] International Atomic Energy Agency. “IAEA Helps Close Radioisotope Production Gap”. In: (2022). Accessed: March 6, 2024. URL: https://www.iaea.org/newscenter/news/iaea-helps-close-radioisotope-production-gap.

[10] JE Beaver and HB Hupf. “Production of ^{99m}Tc on a medical cyclotron: a feasibility study”. In: *Journal of Nuclear Medicine* 12.11 (1971), pp. 739–741.

[11] Serge Rodrigue, Johan E van Lier PhD, and Erik J van Lier MAS. “Cyclotron production of ^{99m}Tc: an approach to the medical isotope crisis”. In: *The Journal of Nuclear Medicine* 51.4 (2010), 13N.

[12] Steven C Van der Marck, Arjan J Koning, and Kevin E Charlton. *The options for the future production of the medical isotope 99 Mo*. 2010.

[13] SM Qaim et al. “Evaluation of excitation functions of ^{100}Mo(p,d+pn) ^{99}Mo and ^{100}Mo (p,2n) ^{99m}Tc reactions: estimation of long-lived Tc-impurity and its implication on the specific activity of cyclotron-produced ^{99m}Tc”. In: *Applied Radiation and Isotopes* 85 (2014), pp. 101–113.

[14] Nuclear Power. *Transient Equilibrium*. https://www.nuclear-power.com/nuclear-power/reactor-physics/atomic-nuclear-physics/radioactive-decay/radioactive-equilibrium/transient-equilibrium/. Accessed: 2024-06-06. 2024.

[15] J. Bashyal. *Molybdenum (Mo) - Element Properties*. Accessed: 31 May 2024. URL: https://scienceinfo.com/molybdenum-mo-element-properties/.

[16] Draw.io. Accessed on: 03-04-2024. URL: https://app.diagrams.net/.

[17] Nikolay Uzunov et al. “Quality assurance of Mo-99/Tc-99m radionuclide generators”. In: *Acta Scientifica Naturalis* 5.1 (2018), pp. 40–47. DOI: 10.2478/asn-2018-0006.

[18] Mohamed F Nawar and Andreas Türler. “New strategies for a sustainable 99mTc supply to meet increasing medical demands: Promising solutions for current problems”. In: *Frontiers in Chemistry* 10 (2022). DOI: https://doi.org/10.3389/fchem.2022.926258.

[19] IAEA. *^{99}Mo → ^{99m}Tc radionuclide principles*. Accessed: March 12, 2024. 2016. URL: https://humanhealth.iaea.org/HHW/Radiopharmacy/VirRad/Eluting_the_Generator/Generator_Module/99Mo_-_99mTc_radionuclide_principles/index.html.

[20] Ashutosh Dash, F.F. (Russ) Knapp, and M.R.A. Pillai. “^{99}Mo/^{99m}Tc separation: An assessment of technology options”. In: *Nuclear Medicine and Biology* 40.2 (2013), pp. 167–176. ISSN: 0969-8051. DOI: https://doi.org/10.1016/j.nucmedbio.2012.10.005.

[21] Sankha Chattopadhyay and Malay Kanti Das. “A novel technique for the effective concentration of ^{99m}Tc from a large alumina column loaded with low specific-activity (n,γ)-produced ^{99}Mo”. In: *Applied Radiation and Isotopes* 66.10 (2008), pp. 1295–1299. ISSN: 0969-8043. DOI: https://doi.org/10.1016/j.apradiso.2008.02.085.

[22] Mohamed F Nawar et al. “Developing a Chromatographic 99mTc Generator Based on Mesoporous Alumina for Industrial Radiotracer Applications: A Potential New Generation Sorbent for Using Low-Specific-Activity 99Mo”. In: *Molecules* 27 (2022), p. 5667. DOI: 10.3390/molecules27175667.

[23] Ananthakumar Ramadoss et al. “Enhanced activity of a hydrothermally synthesized mesoporous MoS_2 nanostructure for high performance supercapacitor applications”. In: *New Journal of Chemistry* 38.6 (2014), pp. 2379–2385.

[24] Meng Wang et al. “Enhanced lithium storage performances of hierarchical hollow MoS_2 nanoparticles assembled from nanosheets”. In: *ACS applied materials & interfaces* 5.3 (2013), pp. 1003–1008.

[25] Xu Wu et al. “Engineering stable and fast sodium diffusion route by constructing hierarchical MoS_2 hollow spheres”. In: *Journal of Colloid and Interface Science* 595 (2021), pp. 43–50.

[26] Lina Wang et al. “Hierarchical hollow MoS_2 nanospheres with enhanced electrochemical properties used as an electrode in supercapacitor”. In: *Electrochimica Acta* 186 (2015), pp. 391–396.

[27] Lei Zhang et al. “Hierarchical MoS_2 microboxes constructed by nanosheets with enhanced electrochemical properties for lithium storage and water splitting”. In: *Energy & Environmental Science* 7.10 (2014), pp. 3302–3306.

[28] Omnia Samy et al. “A review on MoS_2 properties, synthesis, sensing applications and challenges”. In: *Crystals* 11.4 (2021), p. 355.

[29] Department of Chemical Engineering IIT Kanpur. *X-ray diffraction (xrd)*. URL: https://www.iitk.ac.in/che/PG_research_lab/pdf/resources/XRD-reading-material.pdf.

[30] Beverley J Inkson. “Scanning electron microscopy (SEM) and transmission electron microscopy (TEM) for materials characterization”. In: *Materials characterization using nondestructive evaluation (NDE) methods*. Elsevier, 2016, pp. 17–43.

[31] Jonathon A Brame and Christopher S Griggs. “Surface area analysis using the Brunauer-Emmett-Teller (BET) method: scientific operation procedure series: SOP-C”. In: (2016).

[32] Glenn F Knoll. *Radiation detection and measurement*. John Wiley & Sons, 2010.

[33] Perkin Elmer Instruments. “The 30-Minute Guide to ICP-MS”. In: *USA. Disponível em: http://las.perkinelmer. com/Content/TechnicalInfo/TCH_ICPMSThirtyMinuteGuide. pdf* (2001).

[34] Biorender. 2024. URL: https://www.biorender.com/.

[35] *ImageJ. Imagej image processing and analysis in java, 2022.*

[36] EI Pogorel’tsev et al. “Thermodynamic properties and structure of oxyfluorides $Rb_2KMoO_3F_3$and $K_2NaMoO_3F_3$”. In: *Physics of the Solid State* 53 (2011), pp. 1202–1211.

[37] Hao Luo et al. “Hydrothermal synthesis of hollow MoS_2 microspheres in ionic liquids/water binary emulsions”. In: *Materials letters* 62.20 (2008), pp. 3558–3560.

[38] Stephen P Huestis. “Understanding the origin and meaning of the radioactive decay equation”. In: *Journal of Geoscience Education* 50.5 (2002), pp. 524–527.

[39] Alexey Kabalnov. “Ostwald ripening and related phenomena”. In: *Journal of Dispersion Science and Technology* 22.1 (2001), pp. 1–12. DOI: https://doi.org/10.1081/DIS-100102675.

[40] Science Info. *Nitric Acid (HNO3) - Properties, Reactions, Applications, Preparation and Uses*. Accessed: 2024-06-09. 2024. URL: https://scienceinfo.com/nitric-acid-hno3-properties-reactions/.

[41] Qiao Zhang et al. “Self-templated synthesis of hollow nanostructures”. In: *Nano Today* 4.6 (2009), pp. 494–507.

[42] Matthias Kick, Philipp Keil, and Axel König. “Solid–liquid phase diagram of the two Ionic Liquids EMIMCl and BMIMCl”. In: *Fluid Phase Equilibria* 338 (2013), pp. 172–178.

[43] Isabela Alves De Castro et al. “Molybdenum oxides–from fundamentals to functionality”. In: *Advanced Materials* 29.40 (2017), p. 1701619. DOI: https://doi.org/10.1002/adma.201701619.

[44] Zhibin Song et al. “Thermally regulated molybdate-based ionic liquids toward molecular oxygen activation for one-pot oxidative cascade catalysis”. In: *Green Chem.* 22 (2020), pp. 103–109. DOI: 10.1039/C9GC03646F.

[45] Min Wang et al. “Highly selective and efficient adsorption dyes self-assembled by 3D hierarchical architecture of molybdenum oxide”. In: *RSC advances* 5.104 (2015), pp. 85248–85255.

[46] Ali Khademi et al. “Growth and field emission study of molybdenum oxide nanostars”. In: *The Journal of Physical Chemistry C* 113.44 (2009), pp. 19298–19304.

[47] Sergio Puebla et al. “Optical-based thickness measurement of MoO3 nanosheets”. In: *Nanomaterials* 10.7 (2020), p. 1272.

[48] Eleonora Pavoni et al. “First-principles calculation of MoO2 and MoO3 electronic and optical properties compared with experimental data”. In: *Nanomaterials* 13.8 (2023), p. 1319.

[49] Naoko I Kato. “Reducing focused ion beam damage to transmission electron microscopy samples”. In: *Journal of electron microscopy* 53 (2004), pp. 451–458. DOI: doi:10.1093/jmicro/dfh080.

[50] Xiuling Zhang et al. “Controllable constructing of hollow MoS_2/PANI core/shell microsphere for energy storage”. In: *Applied Surface Science* 460 (2018), pp. 48–57.

[51] U.S. Department of Labor. *Occupational Safety and Health Standards*. https://www.govinfo.gov/link/cfr/29/1910?link-type=pdf&sectionnum=1000&year=mostrecent. Accessed on 27-05. 2023.

[52] Luchuan Chen, Wenjun Gu, and Xuanyu Zhang. “Environment effect on the rutting resistance of nano-SiO2-modified asphalt concrete: temperature and water”. In: *Advances in Civil Engineering* 2021 (2021), pp. 1–9. DOI: https://doi.org/10.1155/2021/7439006.

[53] Gauri. “Designing a Recyclable Low-Specific Activity ^{99}Mo/^{99m}Tc Generator”. PhD Proposal. PhD thesis. Delft University of Technology, Jan. 2023.

[54] Victor J Molinski. “A review of 99mTc generator technology”. In: *The International Journal of Applied Radiation and Isotopes* 33.10 (1982), pp. 811–819.

[55] Riya Gupta and Muhammad F Hashmi. “Mo99-Tc99m Generator”. In: (2020).

[56] International Atomic Energy Agency (IAEA). *Live Chart of Nuclides*. 2024. URL: %5Curl%7Bhttps://www-nds.iaea.org/relnsd/vcharthtml/VChartHTML.html%7D.

[57] Stefaan Pomme, R Fitzgerald, and J Keightley. “Uncertainty of nuclear counting”. In: *Metrologia* 52 (2015). DOI: DOI10.1088/0026-1394/52/3/S3.

[58] GQ Lu and XS Zhao. “Nanoporous materials: An overview”. In: *Nanoporous materials: science and engineering* 4 (2004), pp. 1–12.

[59] B. Spivakov and V. Shkinev. “Membrane Techniques | Ultrafiltration”. In: *Encyclopedia of Analytical Science (Second Edition)*. Ed. by Paul Worsfold, Alan Townshend, and Colin Poole. Elsevier, 2005, pp. 524–530. DOI: https://doi.org/10.1016/B0-12-369397-7/00368-X.

[60] Xiaochuan Duan et al. “The art of using ionic liquids in the synthesis of inorganic nanomaterials”. In: *CrystEngComm* 16.13 (2014), pp. 2550–2559. DOI: DOI:10.1039/C3CE41203B.

[61] Ashutosh Dash, FF Russ Knapp Jr, and MRA Pillai. “99Mo/99mTc separation: An assessment of technology options”. In: *Nuclear medicine and biology* 40 (2013), pp. 167–176. DOI: http://dx.doi.org/10.1016/j.nucmedbio.2012.10.005.

[62] Amogh Ananda Rao and Smilee Johncy. “Tennis courts in the human body: a review of the misleading metaphor in medical literature”. In: *Cureus* 14 (2022). DOI: 10.7759/cureus.21474.

A

Appendix

Synthesis of KF

NH_4F and KOH were mixed in a milliQ solution. In the solutions, NH_4(g) will be present together with F^-, K^+ and OH^- ions. F^- and K^+ will form a strong ionic bond to form KF:

$$NH_4F + KOH \rightarrow KF + \begin{cases} NH_4OH(aq) \\ NH_3 \cdot H_2O \\ NH_3(g) + H_2O(l) \end{cases}$$

In a Schlenk line, the sample was put in a vacuum condition and N_2(g) was slowly introduced to the solution. This was done to remove as much of the NH_3 gas as possible, thereby purifying the product. Since N_2 is an inert gas, it will not react with any of the substances in the solution. The reaction mixture was dried at 80 °C for six days.

SEM sample preparation

A thin layer of solid sample is spread on double-sided carbon tape (Electron Microscopy Sciences). It is put in a holder, with which four samples at a time can be imaged.

TEM sample preparation

All TEM samples were made in the following manner: Typically, 0.5 - 1.0 mg of material was dispersed in 500-1000 μL milliQ by bath sonicating it for 2-5 min. With a P20 pipet, 20 μL of the solution was drop-cast on a TEM grid (Formvar/Carbon 200 Mesh Copper, Electron Microscopy Sciences) multiple times to ensure enough product on the grid. Then, the grid is placed in a holder for safekeeping until it the sample is imaged.

B

Images

XRD patterns

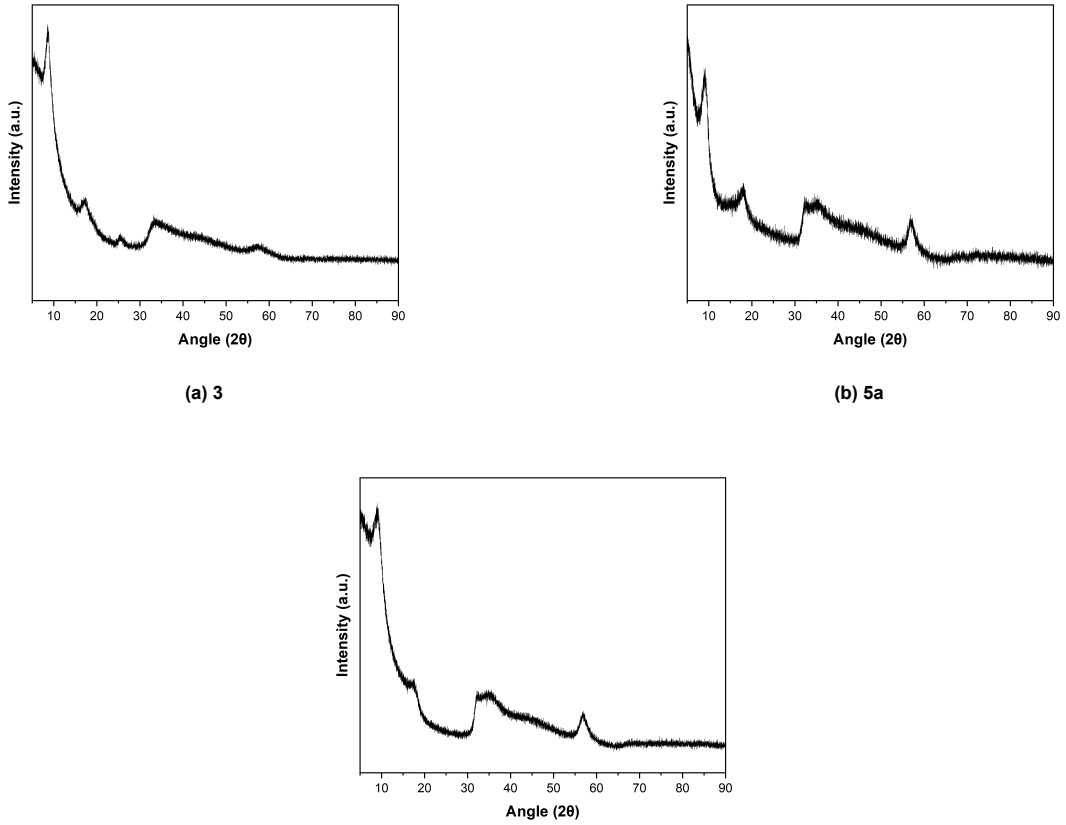

Figure B.1: XRD patterns of MoS_2 materials.

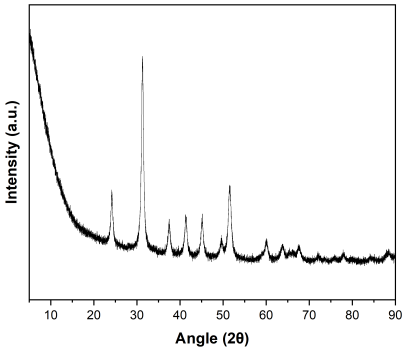

(a) $MnCO_3$ solid spheres

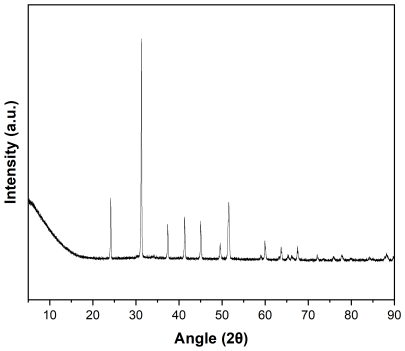

(b) $MnCO_3$ solid cubes

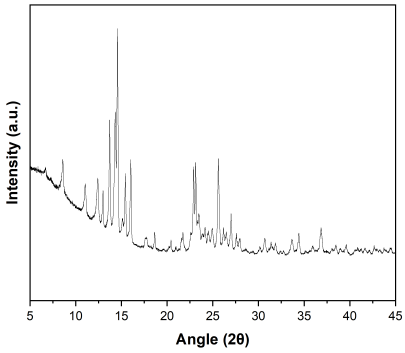

(c) $C_{10}H_{14}MoO_6$ (molybdyl acetoacetonate)

Figure B.2: Additional XRD patterns.

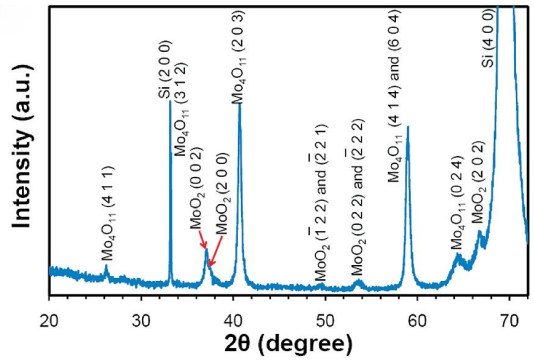

(a) MoO_2 [46].

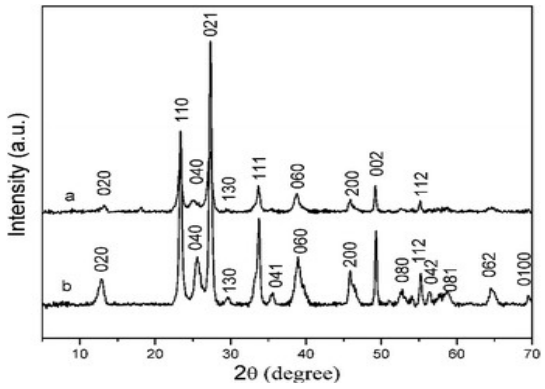

(b) (a) MoO_3, (b) calcinated MoO_3[45].

Figure B.3: XRD patterns of molybdenum oxides found in literature.

SEM images

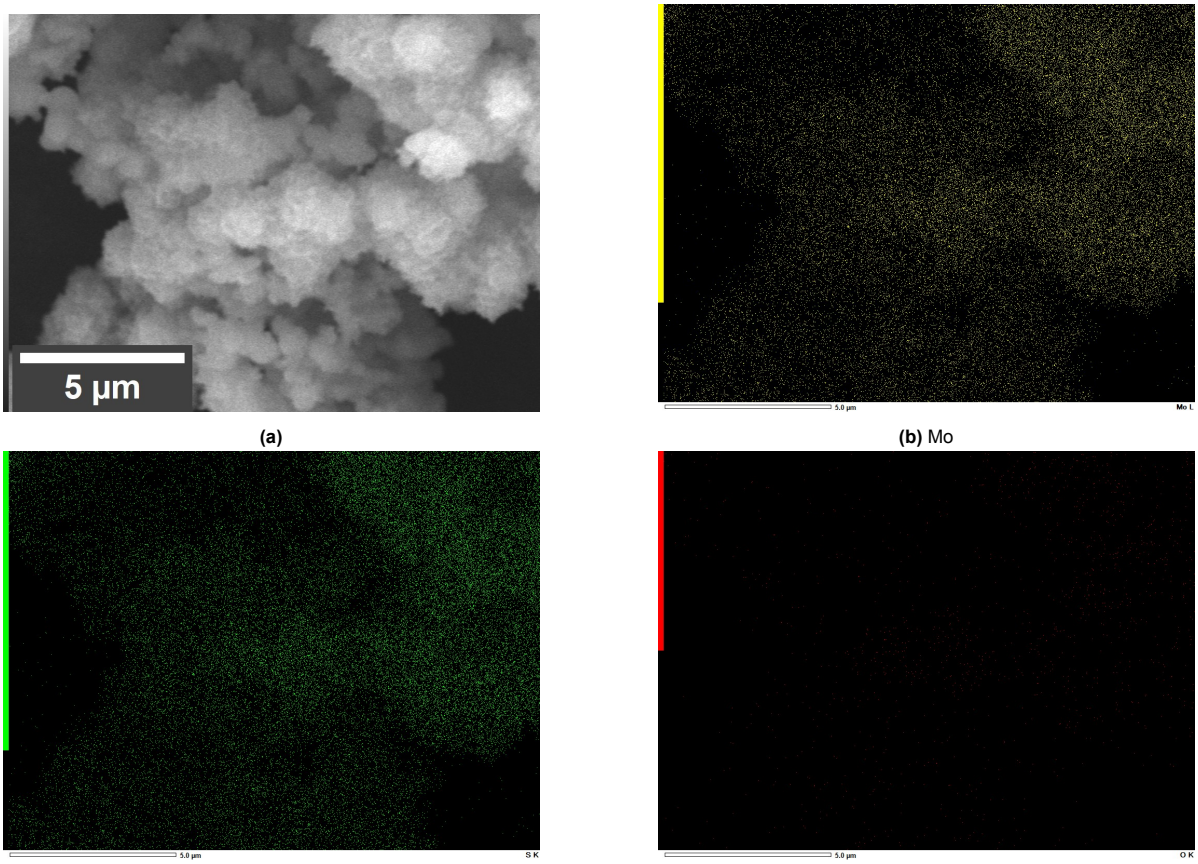

(a)

(b) Mo

(c) S

(d) O

Figure B.4: SEM EDX analysis for **3S**.

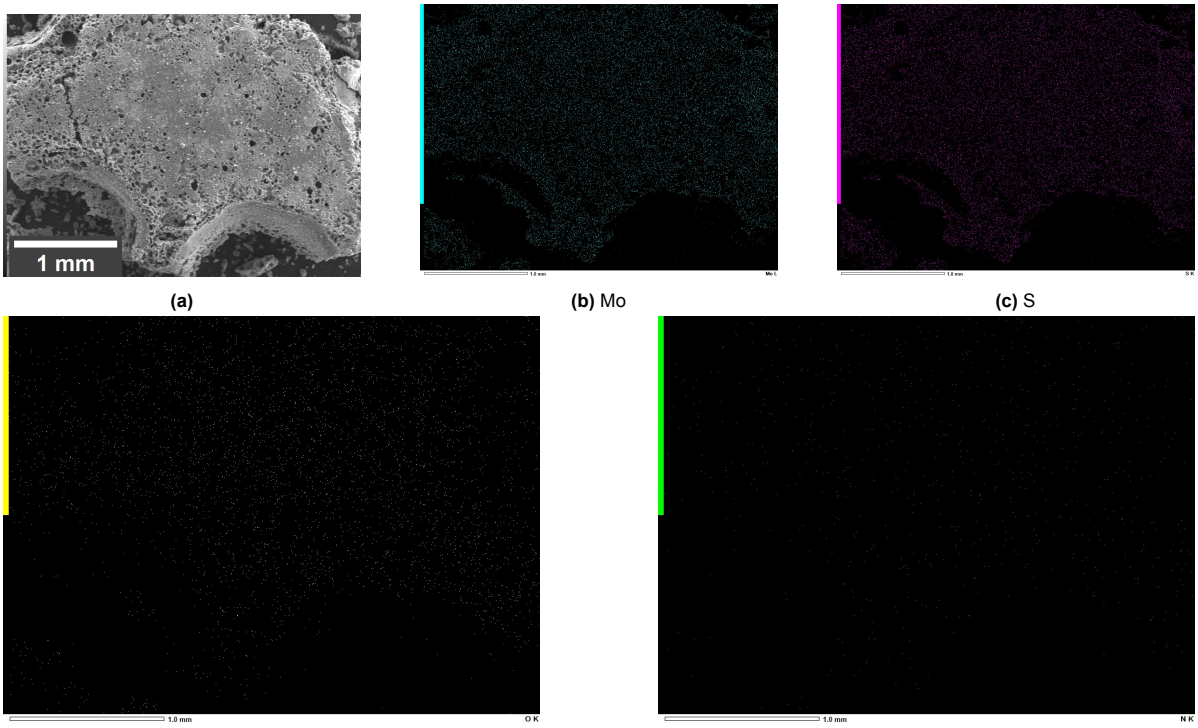

Figure B.5: SEM EDX analysis for **3L**.

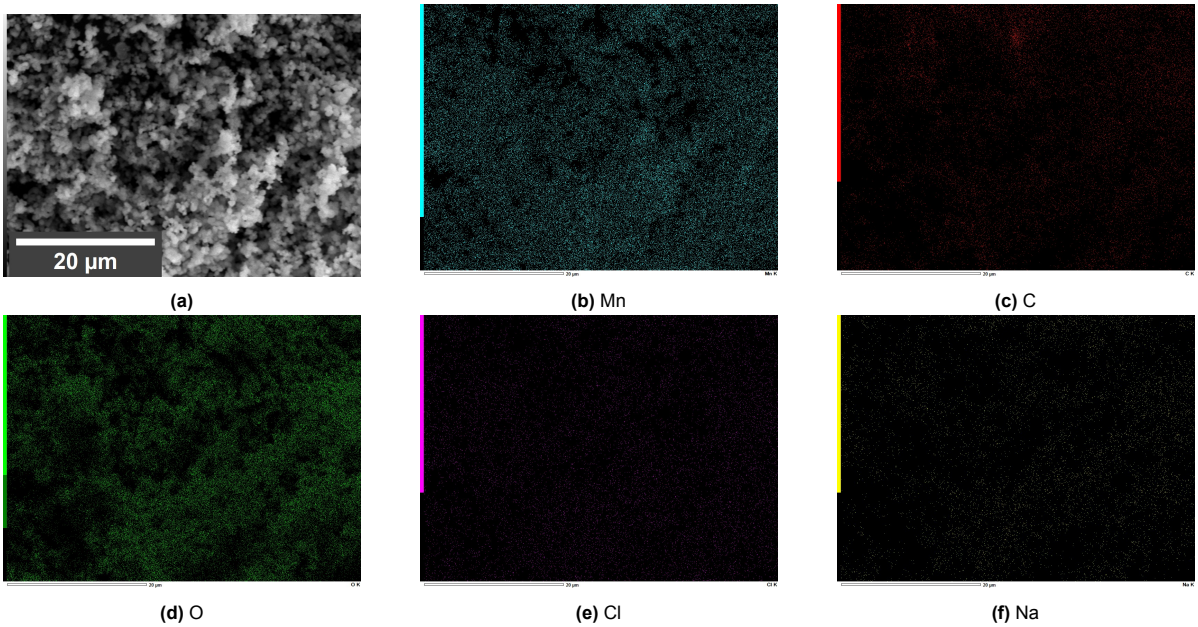

Figure B.6: SEM EDX analysis for **5a $MnCO_3$ spheres**.

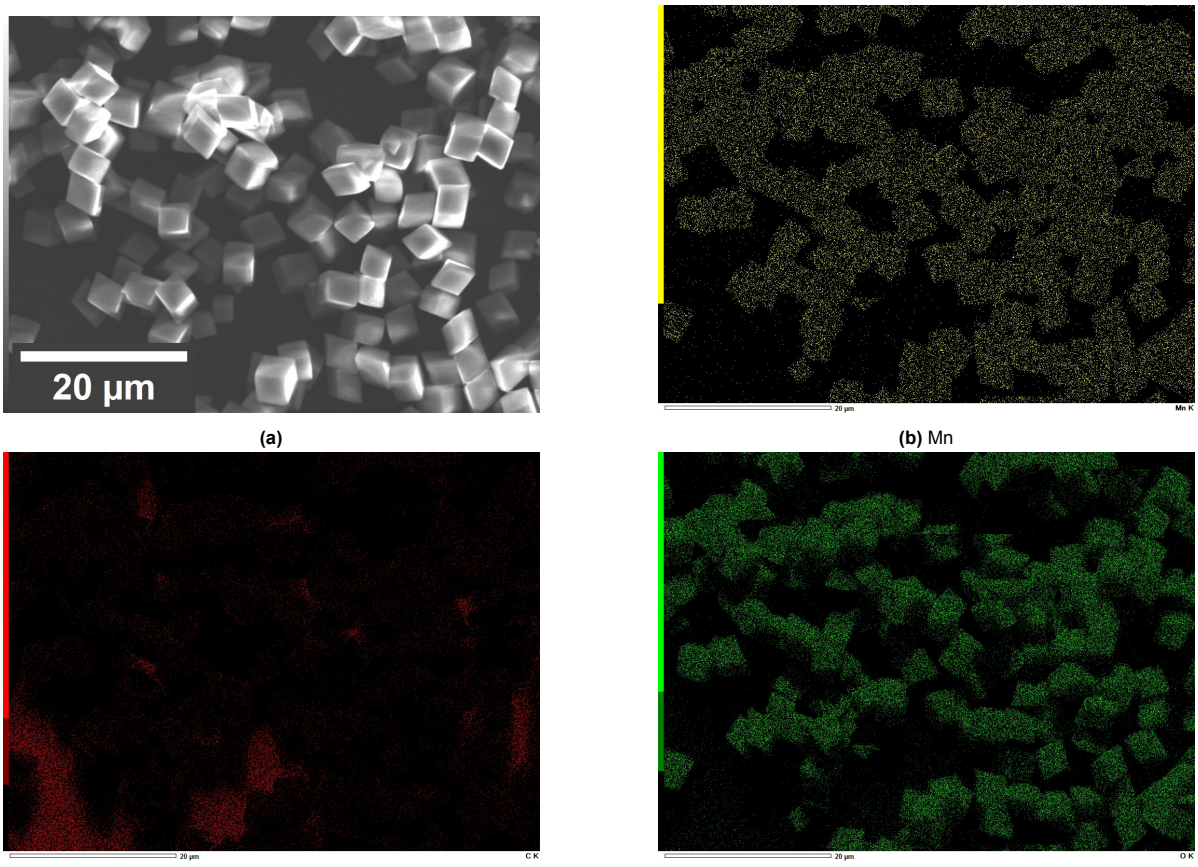

(a) **(b)** Mn

(c) C **(d)** O

Figure B.7: SEM EDX analysis for **5b $MnCO_3$ cubes**.

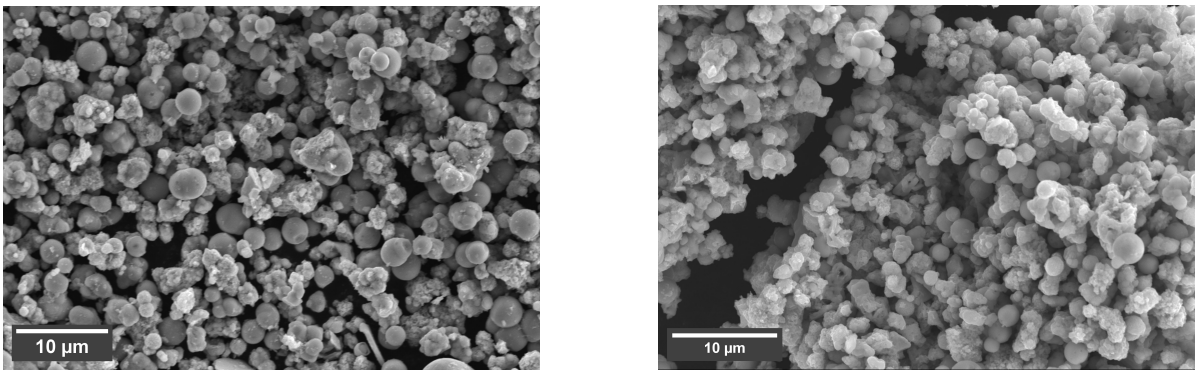

(a) **(b)**

Figure B.8: SEM of **2** before (a) and after (b) stability tests.

TEM images

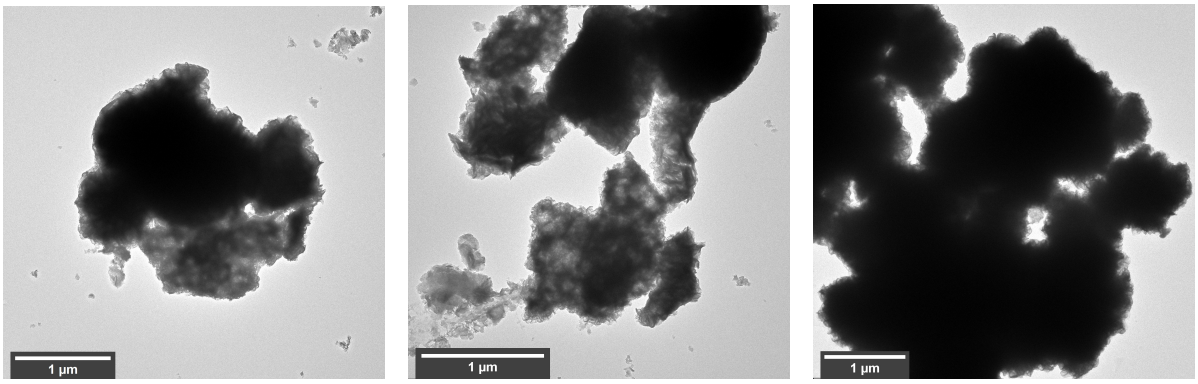

(a) (b) (c)

Figure B.9: 2 double 2 M HCl acid wash.

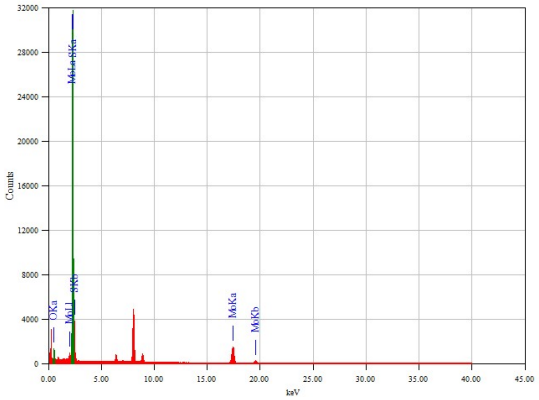

Figure B.10: TEM EDX graph for **2** 0.5 M HNO_3 acid wash.

Table B.1: TEM EDX data of**2** 0.5 M HNO_3 acid wash.

Element	Counts	Mass%	Sigma	Atom%
O	4260.72	0.83	0.01	3.24
S	191376.83	24.66	0.08	48.14
Mo	160270.81	74.51	0.30	48.62

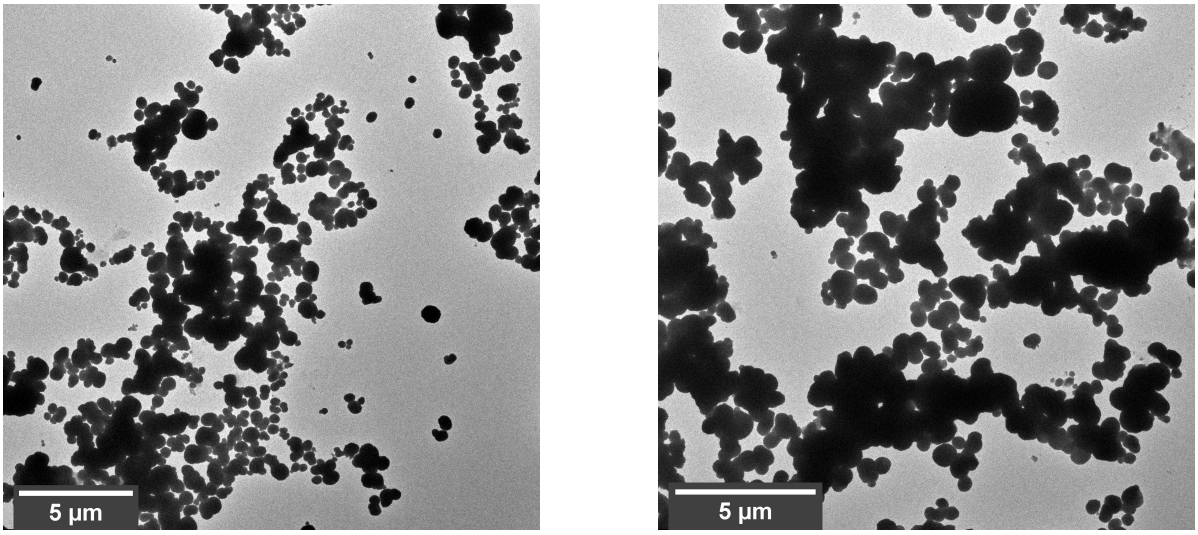

(a) t = 15 min **(b)** t = 30 min

Figure B.11: $MnCO_3$ spheres with different stirring times.

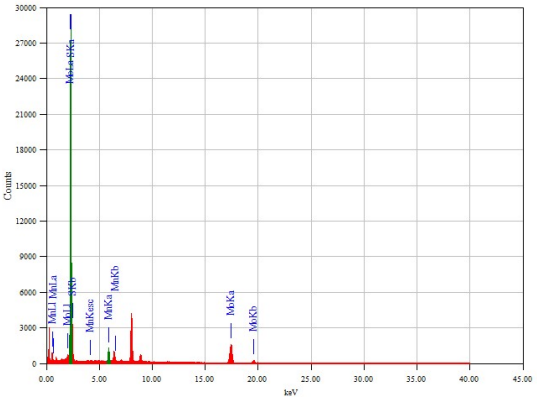

Figure B.12: TEM EDX graph for **5a**.

Table B.2: TEM EDX data of **5a**.

Element	Counts	Mass%	Sigma	Atom%
Mn	15932.38	3.35	0.02	3.69
S	191851.41	28.21	0.08	53.18
Mo	128999.10	68.44	0.31	43.13

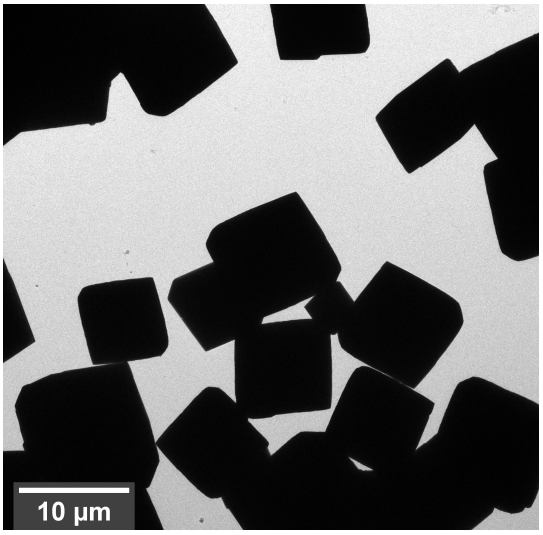

Figure B.13: $MnCO_3$ cubes with t = 16 h heating time.